In situ oxygen, magnesium, and silicon isotopic compositions of the FUN inclusion Vigarano 1623-5

Johanna MARIN-CARBONNE [1,2†]*, Kevin D. MCKEEGAN[1], Andrew M. DAVIS[3,4],
Glenn J. MACPHERSON [5], Ruslan A. MENDYBAEV[3], and Frank M. RICHTER[3]

[1]Department of Earth, Planetary, and Space Sciences, University of California—Los Angeles, Los Angeles, California, USA
[2]Institut des Sciences de la Terre, Université de Lausanne, Lausanne, Switzerland
[3]Department of the Geophysical Sciences, University of Chicago, Illinois, USA
[4]Enrico Fermi Institute, University of Chicago, Chicago, Illinois, USA
[5]Department of Mineral Sciences, National Museum of Natural History, Smithsonian Institution, Washington, DC, USA
[†]Current address: Earth Sciences Institute, University of Lausanne, Lausanne, Switzerland
*Corresponding author.
Johanna Marin-Carbonne, Department of Earth, Planetary, and Space Sciences, University of California—Los Angeles,
Los Angeles, CA 90095, USA.
E-mail: johanna.marincarbonne@unil.ch

Abstract–Oxygen, magnesium, and silicon isotopic abundances in Vigarano 1623-5 were studied using secondary ion mass spectrometry to investigate correlations between isotopic and petrologic properties of this unique forsterite-bearing FUN inclusion. Vigarano 1623-5 displays large, correlated mass-dependent fractionation effects, tightly linked to mineralogy within distinct petrologic units of the inclusion. The pyroxene-rich and melilite-rich interior parts of the inclusion display highly mass-fractionated isotopic compositions of oxygen, magnesium, and silicon, consistent with Rayleigh distillation during evaporation of a melt with initial oxygen composition close to a solar composition. However, the chemical composition, enriched in magnesium and silicon, suggests a precursor already fractionated by prior melt evaporation. A discontinuous igneous rim was produced by a flash-melting event followed by isotopic exchange in the rim melilite with planetary-like oxygen, mechanical fragmentation, and reassembly with an accretionary rim of heterogeneous materials. Al-rich minerals in 1623-5 show evidence for having crystallized with live ^{26}Al but at less than the "canonical" level of most CV calcium-aluminum-rich inclusions. However, well-defined ^{26}Al-^{26}Mg isochrons are not found and temporal implications are ambiguous.

INTRODUCTION

Calcium-aluminum-rich inclusions (CAIs) are the earliest solids known to have formed in the solar nebula, at 4.568 Ga (Amelin et al., 2010; Connelly et al., 2012; Desch et al., 2023; Piralla et al., 2023). The mineralogical and chemical compositions of CAIs indicate that their precursor materials formed in a high-temperature gas of solar composition (Grossman, 1975; Grossman et al., 2002; MacPherson, 2014), probably in the innermost solar system (MacPherson, 2014; McKeegan et al., 2000). Detailed petrographic and isotopic evidence demonstrates that many

inclusions experienced complex thermal histories, involving one or more episodes of partial melting, evaporation, condensation, and transport prior to incorporation in planetesimals (see MacPherson, 2014, for a review). These complex thermal histories reflect the physicochemical environment(s) in which CAIs formed and the nebular processes that affected them.

One rare subset of CAIs, namely those known as "FUN" inclusions in reference to their Fractionated and Unidentified Nuclear isotopic effects (Wasserburg et al., 1977), remains poorly understood. Hallmark characteristics of FUN CAIs include (1) large mass-dependent

isotopic fractionation effects in magnesium, silicon, and oxygen, thought to be the result of melt evaporation with significant mass loss (Davis et al., 1991); (2) relatively large isotope anomalies of apparent nucleosynthetic origin in a wide variety of elements such as calcium, titanium, barium, neodymium, and others (Clayton et al., 1984, 1977; Clayton & Mayeda, 1977; Davis et al., 1991; Lee et al., 1979; MacPherson, 2014); (3) very low or no detectable radiogenic ^{26}Mg from the decay of ^{26}Al (Fahey et al., 1987; MacPherson et al., 1995; Park et al., 2017); and (4) small nonradiogenic isotope anomalies in magnesium (Loss et al., 1994; McKeegan et al., 2005). Given these nucleosynthetic isotope anomalies, the paucity of ^{26}Al in FUN inclusions at the time of last crystallization is commonly interpreted as due to their formation prior to injection of ^{26}Al into the early solar nebula (Fahey et al., 1987; Sahijpal & Goswami, 1998), rather than formation several million years later than non-FUN CAIs.

Only those FUN inclusions from CV3 chondrites are large enough to be suitable for multiple isotopic studies that include bulk methods. Yet even for these, few have been studied in detail either petrologically or via secondary ion mass spectrometry (SIMS). In fact, for the two prototype examples "C1" and "EK-1-4-1" (Lee et al., 1976; Wasserburg et al., 1977), further detailed petrologic studies are no longer even possible because only small grain mounts still exist. One of the classic FUN CAIs that does remain in its petrographic context as a thin section in the host meteorite is Vigarano 1623-5 (Davis et al., 1991; Loss et al., 1994). This object (henceforth, 1623-5) is a forsterite-bearing (FoB) type B CAI, a variety notable for the fact that a disproportionate number have FUN characteristics (Bullock et al., 2012; Clayton et al., 1984; Krot et al., 2010). A remarkable feature of 1623-5 is that it is nearly identical in the isotopic compositions of many elements to the Allende FUN inclusion C1 (Loss et al., 1994); yet, the mineralogy and chemical compositions of the two CAIs are very different. Unlike the forsterite-rich 1623-5, C1 is a type B CAI containing melilite, pyroxene, spinel, and anorthite, but no olivine. The petrography, mineralogy, and chemistry of 1623-5 are described in Davis et al. (1991) and aspects of its isotopic composition are given in Davis et al. (1991) and Loss et al. (1994). Those earlier investigations documented correlated petrologic and isotopic evidence for large degrees of melt evaporation in 1623-5 (Davis et al., 1991; MacPherson et al., 1984), which were later corroborated by melt evaporation experiments that reproduced bulk chemical compositions and oxygen, magnesium, and silicon isotopic composition of 1623-5 and C1 (Mendybaev et al., 2013), but there has been no coordinated SIMS study of mass-dependent isotopic fractionation to examine the details of this process nor has there been any in situ analyses of its oxygen or radiogenic magnesium isotopic properties. Accordingly, we report here the results of a series of SIMS

studies of 1623-5 done intermittently over the past two decades. Our goal is to better constrain the complex petrogenetic history of 1623-5 and thereby gain insights into the origin of FUN CAIs in general. Preliminary results were reported previously in a series of abstracts (Davis et al., 2000; Marin-Carbonne et al., 2011, 2011a, 2011b; Marin-Carbonne, Chaussidon, et al., 2012; Marin-Carbonne, McKeegan, et al., 2012; McKeegan et al., 2005) and some magnesium isotopic data were presented in Davis et al. (2015).

SAMPLE DESCRIPTION

A detailed mineralogical and petrographic description of 1623-5 is given by Davis et al. (1991). In thin section, 1623-5 is ~4 mm across and irregularly shaped; it is composed of two major pieces, one melilite rich and the other pyroxene rich (Figure 1), which are separated by intervening fine-grained accretionary rim material that is refractory rich and Fe poor compared to normal Vigarano matrix. Both parts of the CAI have olivine-rich cores and discontinuous olivine-free rims. The largest part of the CAI is the pyroxene-rich portion. Its core is composed of rounded forsterite crystals, ~30 to 100 μm in size, that are poikilitically enclosed within aluminum-, titanium-rich clinopyroxene, and magnesium-rich melilite (average åkermanite composition is $Åk_{89}$; Davis et al., 1991). This region contains two rounded cavities (one larger and one smaller), thought to be vesicles, that are now filled with accretionary material that is mostly fine-grained with some locally abundant larger hibonite and spinel grains (Figure 2). This accretionary material is distinct from normal Vigarano matrix and appears to be richer in aluminum and calcium with fine-grained hibonite, spinel, and perovskite common. In the core of the melilite-rich portion of 1623-5, pyroxene is essentially absent. Spinel is unevenly distributed throughout both parts of the CAI.

Of particular interest here is the ~200 μm-thick (maximum), olivine-free, discontinuous igneous rim that surrounds the inclusion cores (Figure 1c). The rim consists mainly of aluminum-rich melilite, which shows increasing aluminum content outward, ranging from $Åk_{63}$ to $Åk_{36}$; detached melilite grains lying just outside the solid rim are even more aluminous, down to $Åk_{16}$ (Davis et al., 1991). Like other Vigarano CAIs, 1623-5 shows only minor alteration phases due to secondary, parent-body processes (see Davis et al., 1991).

ANALYTICAL TECHNIQUES

Oxygen, magnesium, and silicon isotope compositions were determined with the CAMECA IMS 1270 ion microprobe at UCLA, using procedures previously described (Aléon et al., 2018; Leshin et al., 1998; Liu
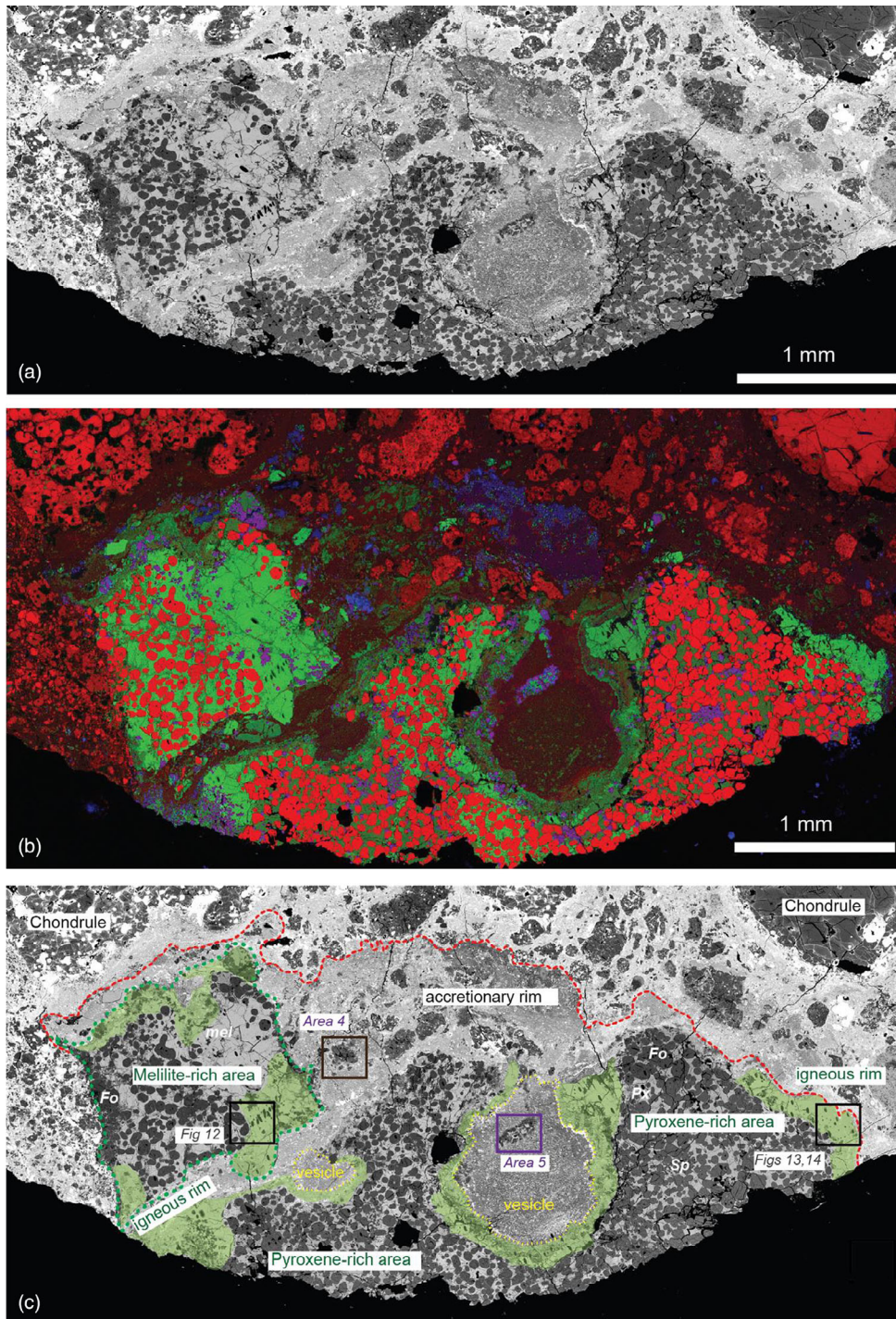
FIGURE 1. a) Back-scattered electron (BSE) image; b) combined elemental map (Mg-red, Ca-green, Al-blue) of Vigarano 1623-5 showing major mineralogy (melilite bright green, forsterite red, spinel purple, and hibonite bright blue); c) BSE image showing large-scale structures of 1623-5. The melilite-rich area (left) is separated from the pyroxene-rich area (right) by fine-grained, refractory (Al-rich) material, interpreted as an accretionary rim. Some of this material also fills a large vesicle in the pyroxene-rich portion. An olivine-free, Al-rich discontinuous igneous rim, present on both the melilite-rich and pyroxene-rich cores, is highlighted in light green. The outer boundary of the aluminum-rich accretionary rim is indicated by the dotted red line, exterior of which lies matrix material of the Vigarano meteorite. Spinel-rich aggregates in Areas 4 and 5 (Figure 2) of the accretionary rim are shown by a purple box.
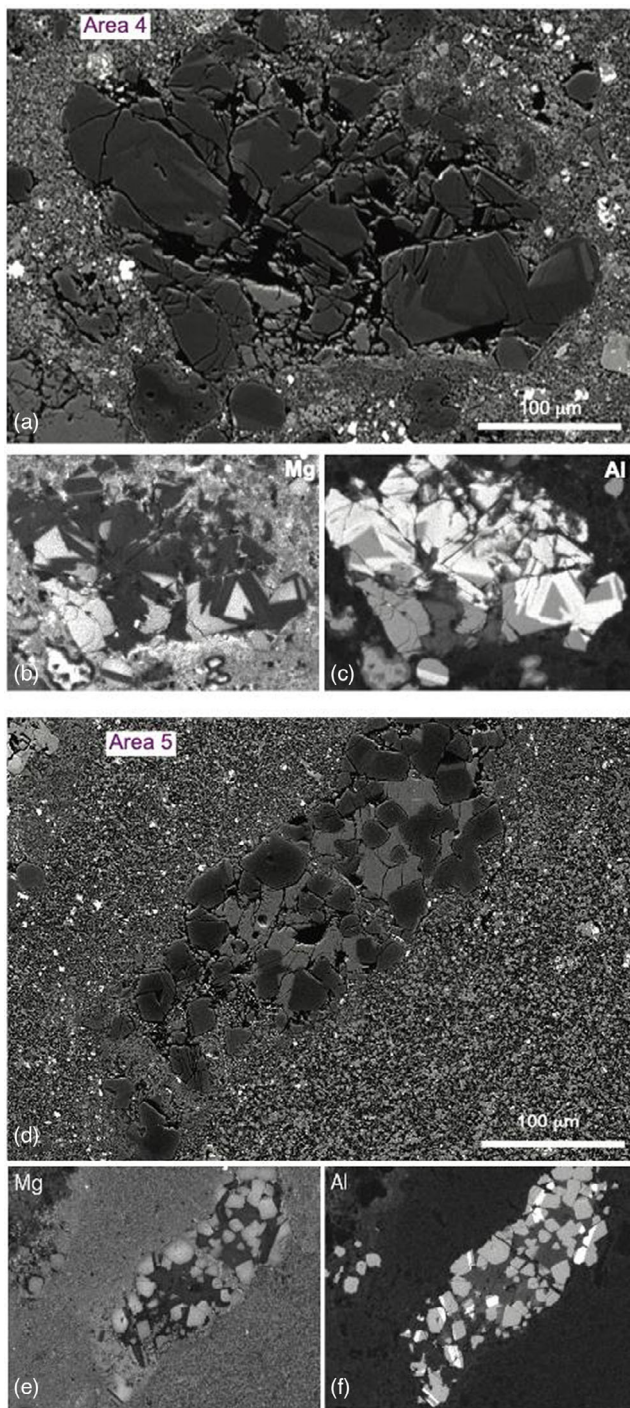
FIGURE 2. BSE images (a, d) and X-ray maps of Mg (b, e) and Al (c, f) of spinel-rich objects in the accretionary rim of 1623-5 from Areas 4 (a–c) and 5 (d–f) indicated by purple boxes in Figure 1c. Area 5 shows euhedral to rounded spinel grains, some with associated hibonite, enclosed within melilite. The scale bar = 100 μm.

et al., 2009; Marin-Carbonne, Chaussidon, et al., 2012; Marin-Carbonne, McKeegan, et al., 2012); specific details are noted below.

Oxygen Isotopes

The samples were sputtered with a ~5 nA, 20 keV Cs^+ primary beam focused to a ~20 μm diameter spot. Charge compensation was achieved by normal incidence electron flooding. Secondary ions were measured at a mass resolving power ($M/\Delta M$) of ~6500. At this mass resolution, the correction for the contribution of the tail of the $^{16}OH^-$ peak to the $^{17}O^-$ was always less than 0.5‰, thus contributing negligible uncertainty to the $\delta^{17}O$ measurements. $^{16}O^-$ was measured on a Faraday cup (FC) and $^{17}O^-$ and $^{18}O^-$ were measured on an electron multiplier by magnetic field peak switching. Ion intensities were corrected for background (FC) and deadtime (EM) and relative detector efficiency (EM/FC yield). Oxygen isotope ratios are reported as $\delta^{17}O$ and $\delta^{18}O$ in ‰ deviations from the Standard Mean Ocean Water (SMOW), and as deviation from the terrestrial fractionation (TF) line as $\Delta^{17}O = \delta^{17}O - 0.52 \times \delta^{18}O$.

Instrumental mass fractionation (IMF) was calibrated by analyzing San Carlos olivine and Burma spinel as primary standards. Systematic errors in the IMF correction, due to differences in the major element compositions of the unknowns from that of the standards, could possibly lead to inaccuracies in a calculated isotopic composition relative to the SMOW scale. However, under our analytical conditions (i.e., low energy secondary ions), such "matrix effects" have been shown to be <1‰ per atomic mass unit (amu) between refractory oxide and silicate minerals with low Fe contents (Simon et al., 2000). Subsequent to the oxygen isotope analyses of 1623-5, we checked for matrix effects in melilite by analyzing standards of widely varying åkermanite content that had become available to us; however, no significant matrix effect (>1‰ per amu) could be resolved (Figure 3b). Thus, data for pyroxene, hibonite, and melilite are reported with no additional corrections applied for possible matrix effects since any such systematic errors would be smaller than the measurement precision. Finally, it is worth noting that because they affect only the magnitude of the IMF, any matrix effects introduce no measurable error on $\Delta^{17}O$, the deviation from the terrestrial mass-dependent fractionation line. The reported uncertainties include both the internal measurement precision on an individual analysis and the external (spot-to-spot) reproducibility for the standard during an analytical session which for San Carlos olivine was typically 0.7‰ for $\delta^{18}O$ and 0.8‰ for $\delta^{17}O$ (2σ).

Magnesium Isotopes

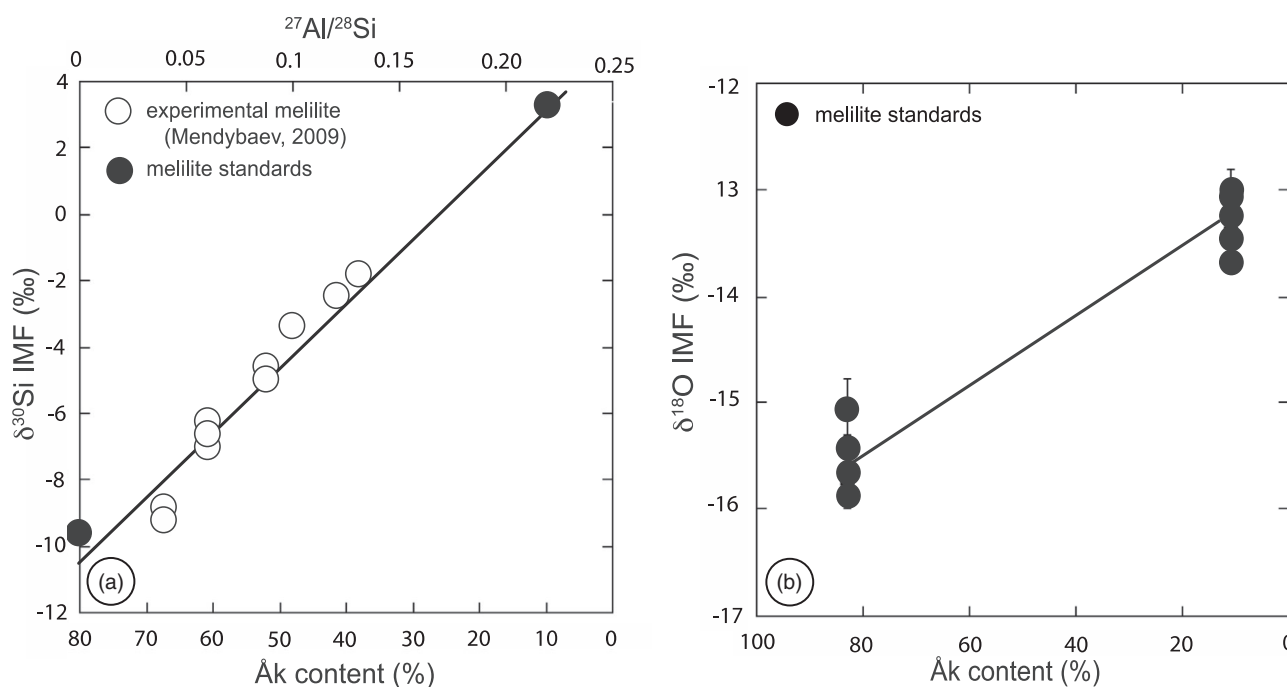Magnesium isotope ratios were measured in multiple sessions. The first session utilized an $^{16}O^-$ primary ion

FIGURE 3. Apparent $\delta^{30}Si$ (a) and $\delta^{18}O$ (b), uncorrected for IMF, plotted against the åkermanite content in melilite standards (solid black symbols) and in a set of experimentally produced zoned melilite crystals (open symbols). A large matrix effect is seen in silicon isotopes as already demonstrated by Knight et al. (2009) but a modest, essentially negligible, matrix effect applies for oxygen over the same range of melilite composition.

beam of 15–20 nA focused to a diameter of 30 μm. The second session prioritized spatial resolution over isotopic precision focusing a 0.6 nA beam to ~10 μm. In each case, the mass resolving power was set at ~4200, sufficient to separate molecular and doubly charged ion interferences ($^{48}Ca^{2+}$ and $^{48}Ti^{2+}$). Ion intensities of $^{27}Al^+$, $^{26}Mg^+$, $^{25}Mg^+$, and $^{24}Mg^+$ were measured simultaneously in multicollection mode by using four Faraday cups ($10^{11}\Omega$ feedback resistors). Measured currents for $^{24}Mg^+$ were ~(4–12) × 10^7 cps equivalent in Session 1 and ~(0.4–2) × 10^7 cps equivalent in Session 2. Ion intensities were corrected for Faraday cup baseline (background) by interpolation of intermittent analyses made with the primary beam blanked. For Session 1, internal precisions of better than 0.1‰ were obtained after few minutes counting (180 s of presputtering to clean the sample surface and establish a steady signal, followed by 35 cycles of 5 s each), whereas precision was generally a factor of 5–20 worse in Session 2 (depending on Mg concentration of the phase analyzed).

Instrumental mass fractionation was corrected for each mineral phase by comparison to analyses (made during the same session) of homogeneous standard materials: San Carlos olivine, Burma spinel, diopside, a glass with composition like the aluminum-, titanium-bearing pyroxene in CAIs, and experimentally produced melilite having a range of compositions. Under our analytical conditions, the magnitude of the IMF for magnesium was up to ~4 to 5‰ per amu different between pyroxene and spinel, with spinel being the most fractionated. Olivine IMF was similar to that of pyroxene (Session 2) or was up to ~3‰ per amu more fractionated (Session 1). In principle, such matrix effects on IMF can also depend on elemental composition even within a given mineral species. In 1623-5, the only mineral phase with large compositional heterogeneity is melilite, and analyses of synthetic melilites spanning a wide compositional range (between $Åk_{10}$ and $Åk_{80}$) showed that matrix effects on IMF for magnesium in melilite are small (<1‰ per amu) under our analytical conditions. Thus, matrix effect corrections were not made for melilites of different Åk content. In addition, for the first session, a melilite standard was not available; in this case, pyroxene glass was used to quantify IMF in melilite. In a similar fashion, Burma spinel was assumed to provide an adequate material for calibrating IMF for magnesium isotopes in hibonite.

Magnesium isotope ratios, corrected for IMF, are reported relative to the DSM3 scale (Galy et al., 2003) as

either $\delta^{25,26}$Mg or using the modified (logarithmic) delta notation adopted from Young and Galy (2004), where

$$\delta^{25}\text{Mg} = 1000 \times \left[\frac{\left(^{25}\text{Mg}/^{24}\text{Mg}\right)\text{sample}}{\left(^{25}\text{Mg}/^{24}\text{Mg}\right)\text{DSM3}} - 1 \right], \quad (1)$$

$$\delta^{25}\text{Mg}' = 1000 \times \ln \left[\frac{\left(^{25}\text{Mg}/^{24}\text{Mg}\right)\text{sample}}{\left(^{25}\text{Mg}/^{24}\text{Mg}\right)\text{DSM3}} \right], \quad (2)$$

and similarly, for δ^{26}Mg and δ^{26}Mg'. The reproducibility for δ^{25}Mg obtained on standard materials ranged between ~0.2‰ (for spinel, pyroxene) and ~0.4‰ for olivine (2σ). The ^{27}Al/^{24}Mg ratio was determined for each spot from the measured ^{27}Al$^+$ and ^{24}Mg$^+$ intensities by applying a relative sensitive factor (RSF) appropriate for the analyzed mineral phase:

$$\left(^{27}\text{Al}/^{24}\text{Mg}\right)_{\text{true}} = \left(^{27}\text{Al}^+/^{24}\text{Mg}^+\right)_{\text{measured}} \times \text{RSF}. \quad (3)$$

The $\left(^{27}\text{Al}/^{24}\text{Mg}\right)_{\text{true}}$ values for each standard were determined from the average of multiple analyses of Al/Mg made with the UCLA JEOL JX-8200 electron microprobe and then correcting for the ^{24}Mg isotope abundance. RSF values were 1.20 for aluminum-, titanium-rich pyroxene (determined on the P0 glass standard) and 1.31 for spinel with 2σ uncertainties of 1.0% and 1.3%, respectively. No pure hibonite phases were analyzed so the spinel RSF was used for spots including mixtures of spinel + hibonite. The RSF for olivine is not well determined because Al concentrations are near or below the detection limit for the electron microprobe. We assigned a value of 1.0 for the olivine RSF; this has no practical consequence for ^{27}Al/^{24}Mg in forsterite of 1623-5 because the Al concentrations are very low.

To calculate the portion of ^{26}Mg that is due to ^{26}Al decay, it is necessary to accurately correct for mass-dependent fractionation that occurred during formation of 1623-5. Following Davis et al. (2015), we used an exponential mass fractionation law with exponent $\beta = 0.5128$. Thus, radiogenic ^{26}Mg* is calculated as:

$$\delta^{26}\text{Mg}^* = \delta^{26}\text{Mg}_{\text{meas}} - \left[\left(1 + \frac{\delta^{25}\text{Mg}_{\text{meas}}}{1000} \right)^{\frac{1}{\beta}} - 1 \right] \times 1000. \quad (4)$$

Because errors on δ^{25}Mg and δ^{26}Mg are highly correlated due to mass fractionation in the analysis and/or in nature, we estimated uncertainty in the determination of radiogenic ^{26}Mg* from the dispersion (i.e., the standard deviation) of standards around the mass-dependent fractionation line. For the high beam intensity session, the standard deviations in the calculated ^{26}Mg* of standards were 0.06‰, 0.05‰, and 0.03‰ for olivine, pyroxene, and spinel, respectively.

Silicon Isotopes

Silicon isotope compositions were measured with a Cs$^+$ primary ion beam and negative secondary ions. For some olivine analyses, silicon isotopes were also measured using an O$^-$ primary beam and analyzing positive secondary ions; however, this method results in higher IMF and yields somewhat lower reproducibility. For most measurements, a Cs$^+$ primary beam of 5 nA and 20 keV impact energy was focused to a diameter of ~30 μm. A normal-incidence electron gun was used for charge compensation. The mass resolving power was set at ~2400 and ^{27}Al$^-$, ^{28}Si$^-$, and ^{30}Si$^-$ were detected simultaneously in multicollection mode with three Faraday cups. Centering of the secondary beam in the field aperture and of the mass peaks on the detectors was done automatically at the start of each analysis. Typical secondary ion intensities for ^{28}Si$^-$ ranged between 4×10^7 cps-equivalent in melilite and 7×10^7 cps-equivalent in olivine, for ^{28}Si$^+$ intensities ranging from 2×10^7 to 5×10^7 for melilite and olivine, respectively. With such conditions, a statistical precision of better than 0.1‰ is obtained after a few minutes of integration (30 s of presputtering followed by 30 cycles of 5 s each). Analyses of a Vigarano chondrule, nearby to 1623-5, were interspersed with the analyses of olivine in the inclusion to monitor for possible drift in the IMF; a dozen analyses showed consistent δ^{30}Si values within 0.1‰. The external (spot-to-spot) reproducibility for δ^{30}Si measurements was 0.34‰ (2σ) and 1.2‰ (2σ) on San Carlos olivine and melilite standard, respectively.

Silicon isotopes are reported as δ^{30}Si and, for positive ion analyses also δ^{29}Si, relative to the standard NBS28, following correction for IMF:

$$\delta^{29,30}\text{Si} = 1000 \times \left[\frac{\left(^{29,30}\text{Si}/^{28}\text{Si}\right)\text{sample}}{\left(^{29,30}\text{Si}/^{28}\text{Si}\right)\text{NBS28}} - 1 \right]. \quad (5)$$

The logarithmic versions, δ^{29}Si' and δ^{30}Si', are defined analogously to the corresponding quantities for magnesium isotopes (Equation 2). Matrix effects on IMF are known to be large for silicon isotopes (Knight et al., 2009; Villeneuve et al., 2019), so careful attention was paid to calibrating the IMF as a function of mineral composition, particularly for melilite which has a wide

range of compositions in 1623-5. We calibrated IMF effects in melilite by analyzing two pure standards having compositions of $\mathring{A}k_{10}$ and $\mathring{A}k_{80}$, and a set of experimentally produced zoned melilites prepared at the University of Chicago. The data (Figure 3a) show that IMF in melilite is reasonably fit by a linear function of åkermanite content with a shift of ~+6.5‰ per amu over the range from $\mathring{A}k_{80}$ to $\mathring{A}k_{10}$, such results found previously by Knight et al. (2009). A much smaller matrix effect exists for oxygen isotopes (Figure 3b), approximately 1‰ per amu between the melilite composition extremes of the standards ($\mathring{A}k_{10}$ and $\mathring{A}k_{80}$). The zoned melilites were not analyzed for $\delta^{18}O$, and a linear interpolation is assumed for intermediate melilites; however, the matrix effect is comparable to the 2σ uncertainties for both $\delta^{18}O$ and $\delta^{17}O$ and thus corrections were not applied.

RESULTS

Oxygen, magnesium, and silicon isotopic compositions of individual grains of forsterite, pyroxene, and melilite, and oxygen and magnesium isotope compositions for spinel and hibonite are reported in Tables 1–3. When possible, we analyzed the same crystal for multiple isotope systems. However, many crystals of 1623-5 were too small to make more than one measurement with our primary beam conditions.

Oxygen Isotopes in 1623-5

Oxygen isotopic compositions were determined in 16 spots of the interior and igneous rim of the pyroxene-rich area of 1623-5 and in three spots in the accretionary materials overlying the inclusion core (Table 1). Data are plotted on three-isotope diagrams in Figure 4a (1623-5 only) and Figure 4b (in comparison with data for other FUN CAIs).

Olivine, spinel, and pyroxene grains are all ^{16}O rich with average $\Delta^{17}O$ values of $-24.2 \pm 0.5‰$, $-25.1 \pm 0.6‰$, and $-24.4 \pm 1.2‰$ (single spot), respectively. The 10 spots measured from the interior of the pyroxene-rich area disperse along a line of slope ~0.5, consistent with mass-dependent fractionation. This line is parallel to but slightly more ^{16}O-enriched than the original "FUN line" put forward by Clayton and Mayeda (1977) based on an evolution from the ^{16}O-rich extreme (i.e., spinel fraction) of "normal" CAIs ($\delta^{18}O = -40‰$, $\delta^{17}O = -42‰$) to the composition ($-20.8‰$, $-31.9‰$) measured in a spinel-rich mineral separate of the "classic" FUN inclusion, EK1-4-1. In 1623-5, spinel from the core plots closest to the ^{16}O mixing line "CCAM" ($\delta^{18}O = -25.1$ to $-15.3‰$) but overlaps significantly with the range of olivine compositions ($\delta^{18}O = -23.8$ to $-8.8‰$); the one analyzed pyroxene spot ($\delta^{18}O = -8.4‰$) is the furthest (i.e., most fractionated) from

TABLE 1. Oxygen isotopic compositions of Vigarano 1623-5.

Spot #	Mineral	$\delta^{18}O$ (‰)	2σ	$\delta^{17}O$ (‰)	2σ	$\Delta^{17}O$ (‰)	2σ
Pyroxene-rich area							
1	Olivine	−20.9	2.4	−35.2	1.6	−24.3	1.8
2	Olivine	−15.6	2.6	−33.3	2.2	−25.3	2.4
3	Pyroxene	−8.4	3.2	−28.8	2.2	−24.4	2.4
7	Olivine	−8.8	3.8	−27.7	3.2	−23.2	3.6
8	Olivine	−14.0	3.6	−32.0	3.0	−24.7	3.4
9	Olivine	−23.8	2.6	−35.3	3.2	−23.0	3.4
6	Spinel	−19.3	2.4	−35.9	2.0	−25.8	2.2
10	Olivine	−11.4	2.6	−29.4	2.4	−23.4	3.0
15	Spinel	−25.1	2.8	−37.7	2.8	−24.6	3.0
16	Spinel	−15.3	2.0	−32.9	2.6	−25.0	2.6
Igneous rim							
4	Melilite	6.2	2.8	−1.5	2.2	−4.7	2.4
5	Melilite	9.5	2.8	1.2	1.6	−3.8	1.8
11	Melilite	9.0	2.0	1.5	2.8	−3.2	2.8
12	Melilite	4.2	3.0	−2.1	3.4	−4.3	3.6
13	Melilite	5.8	1.4	−0.5	2.8	−3.5	3.0
14	Melilite	3.1	2.4	−2.5	2.8	−4.1	2.8
Accretionary rim/vesicle							
17	Spinel aggr.	−23.8	2.6	−38.0	3.0	−25.6	3.4
18	Spinel aggr.	−16.8	2.8	−32.0	3.2	−23.2	3.8
19	Fine-grained	−27.0	2.0	−27.4	2.8	−13.4	3.2

CCAM. Two spots on spinel from an olivine-free spinel-rich aggregate in the large vesicle (Figure 2b) have oxygen isotopic compositions overlapping those of spinel in the interior of the pyroxene-rich area of 1623-5.

In contrast to these primary phases, all melilites from the igneous rim are relatively ^{16}O-depleted and plots along a line parallel to but slightly below the TF line and displaced to the right of CCAM (Table 1 and Figure 4a). The average $\Delta^{17}O$ of the melilite in the rim is $-3.9 \pm 0.5‰$, which is consistent with the melilite fraction measured in EK1-4-1 ($-3.4‰$) and for data from the black rim of the FUN inclusion HAL ($-3.9‰$). The melilite data show a small degree of mass fractionation, which is resolvable beyond what could be plausibly considered as due to matrix effects on the IMF. $\delta^{18}O$ values (for analytical spots hitting only "clean" melilite) range from $+4.2$ to $+9.5‰$, with the heavier (higher $\delta^{18}O$) values at the interior portions of the rim. One melilite point at $+3.2‰$ overlapped slightly onto accretionary rim material. The only other analyzed spot to show relatively ^{16}O-depleted compositions ($\Delta^{17}O = -13.4 \pm 1.6‰$) is from the spinel-rich fine-grained accretionary material immediately adjacent to Vigarano matrix.

Our data on 1623-5 are consistent with more recent ion microprobe data (Figure 4b) obtained on a suite of FUN

TABLE 2. Magnesium isotopic compositions of Vigarano 1623-5.

Spot	Phase	Al/^{24}Mg	1 s	δ^{26}Mg′	2σ	δ^{25}Mg′	2σ	δ^{26}Mg*	2σ
Pyroxene-rich area									
1	fo	0.01	0.09	45.65	0.86	23.66	0.44	−0.50	0.12
2	fo	0.08	0.06	48.23	0.86	24.85	0.46	−0.24	0.12
3	sp (+pyx)	2.19	0.01	62.86	0.86	32.41	0.42	−0.36	0.08
7	fo (+pyx)	0.05	0.05	51.76	0.86	26.80	0.48	−0.54	0.12
9	pyx	0.62	0.04	56.28	0.86	29.01	0.42	−0.30	0.10
10	fo	0.00	0.05	54.98	0.86	28.39	0.44	−0.41	0.12
11	pyx	0.84	0.02	58.12	0.86	29.93	0.42	−0.27	0.10
14	pyx (+fo)	0.17	0.03	52.67	0.86	27.19	0.50	−0.39	0.10
32	fo	0.04	0.08	55.74	0.86	28.79	0.42	−0.44	0.12
B1	fo	0.00	0.01	54.54	1.16	28.64	0.76	−1.40	0.91
B2	fo	0.14	0.02	53.52	1.32	27.23	0.96	0.44	1.09
B3	fo	0.06	0.01	51.49	1.24	26.84	0.88	−0.90	1.00
B4	fo	0.02	0.01	48.94	1.14	25.36	0.64	−0.53	0.86
B5	fo	0.00	0.01	51.57	1.26	27.01	0.92	−1.16	1.02
B6	fo	0.00	0.02	53.00	1.34	27.00	0.94	0.38	1.11
B7	fo	0.00	0.01	51.04	1.22	26.53	0.35	−0.74	0.96
B8	fo	0.02	0.01	47.86	1.12	24.65	0.68	−0.22	0.85
B9	fo (+sp)	0.45	0.01	53.14	1.20	27.17	0.88	0.16	0.93
B10	fo	0.03	0.01	48.91	1.16	25.20	0.68	−0.23	0.90
B11	fo	0.07	0.01	50.56	1.24	25.90	0.72	0.07	1.00
B13	fo	0.00	0.01	43.80	1.16	22.56	0.70	−0.20	0.89
B14	fo	0.00	0.01	42.87	1.14	21.60	0.68	0.78	0.87
B37	pyx	0.01	0.01	52.52	2.66	27.22	1.64	−0.59	4.06
B38	pyx	0.79	0.01	56.28	2.64	28.73	1.72	0.27	4.04
Melilite-rich area									
4	pyx	1.89	0.01	63.37	0.86	32.58	0.44	−0.18	0.10
5	sp	2.58	0.01	62.75	0.86	32.36	0.42	−0.37	0.06
6	fo	0.02	0.08	45.30	0.86	23.48	0.44	−0.50	0.12
18	mel	0.46	0.02	52.56	0.86	27.09	0.42	−0.28	0.10
27	fo	0.07	0.03	44.42	0.86	23.04	0.44	−0.53	0.12
28	fo	0.03	0.11	46.92	0.86	24.23	0.42	−0.35	0.12
29	fo	0.01	0.03	49.39	0.86	25.57	0.42	−0.51	0.12
30	fo	0.02	0.07	50.58	0.86	26.17	0.42	−0.48	0.12
31	fo	0.06	0.06	54.57	0.86	28.22	0.44	−0.49	0.12
B15	fo	0.01	0.01	44.59	1.16	22.79	0.70	0.16	0.90
B16	fo	0.01	0.01	37.55	1.18	19.28	0.70	−0.06	0.93
B17	fo	0.01	0.01	46.44	1.16	23.65	0.70	0.34	0.89
B18	fo	0.00	0.01	46.95	1.12	24.08	0.68	0.00	0.85
B19	fo	0.02	0.01	40.82	1.18	20.76	0.70	0.35	0.92
B22	mel	0.36	0.02	47.34	2.66	24.20	1.86	0.15	4.06
B23	mel	0.50	0.02	53.25	2.70	27.81	1.80	−1.04	4.08
B24	mel	0.89	0.02	48.66	2.68	25.45	1.76	−1.02	4.07
B25	mel	0.90	0.02	49.79	2.78	25.03	1.84	1.03	4.13
Igneous rim—pyroxene-rich area									
12	mel	0.40	0.02	54.98	0.86	28.38	0.42	−0.38	0.10
13	mel	0.39	0.01	56.69	0.86	29.30	0.44	−0.48	0.10
23	pyx	1.46	0.01	57.04	0.86	29.34	0.44	−0.18	0.10
B30	mel	3.19	0.03	52.13	3.06	27.08	2.24	−0.72	4.33
B31	mel	3.00	0.03	50.03	3.10	23.20	2.26	5.01	4.36
B32	mel	2.77	0.03	44.63	3.08	21.52	2.22	2.78	4.34
B33	mel	0.31	0.02	56.44	2.80	28.43	1.88	1.05	4.15
B34	mel	0.34	0.02	50.42	2.80	27.11	1.84	−2.57	4.15
B35	mel	1.00	0.02	52.34	2.86	27.17	1.92	−0.69	4.18

TABLE 2. *Continued*. Magnesium isotopic compositions of Vigarano 1623-5.

Spot	Phase	Al/^{24}Mg	1 s	δ^{26}Mg′	2σ	δ^{25}Mg′	2σ	δ^{26}Mg*	2σ
B36	mel	2.15	0.02	50.63	2.80	24.23	1.84	3.54	4.15
Igneous rim—melilite-rich area									
15	pyx	2.21	0.01	63.12	0.86	32.36	0.42	0.02	0.10
16	sp	2.78	0.01	75.93	0.86	39.00	0.40	−0.13	0.06
17	pyx	3.38	0.01	60.33	0.86	30.98	0.44	−0.09	0.10
Accretionary rim									
19	sp	2.94	0.01	80.44	0.86	41.17	0.42	0.18	0.10
20	sp	2.61	0.01	76.80	0.86	39.29	0.42	0.20	0.06
21	Sp (fine grained)	1.53	0.01	8.89	0.84	4.51	0.42	0.09	0.06
24	vesicle	0.38	0.04	7.65	0.84	3.95	0.42	−0.06	0.12
25	hib (+sp)	3.50	0.03	76.04	0.86	38.93	0.44	0.14	0.06
26	hib	10.88	0.04	65.64	0.86	33.42	0.48	0.50	0.06
Chondrule									
8	fo	0.00	0.07	−0.04	0.84	0.05	0.44	−0.14	0.12
22	fo	0.00	0.03	−0.08	0.84	0.03	0.44	−0.14	0.12

inclusions by Krot et al. (2014) and Williams et al. (2017). The ensemble of the ion microprobe data for spinel and forsterite from the FUN inclusions Axtell 227, B7F6, C1, EK1-4-1, CG-14, and 1623-5 all plot on a single mass-dependent fractionation line (slope = 0.518 ± 0.019; reduced χ^2 = 0.3) which intercepts the CCAM line at approximately δ^{18}O = −46.6‰, δ^{17}O = −48.2‰ (Δ^{17}O = −24.0‰). Many ion microprobe analyses of primary CAI minerals that appear not to have exchanged with an external reservoir plot on the CCAM line at Δ^{17}O = −24 ± 2‰ (e.g., Krot et al., 2020). Although more ^{16}O-enriched than normal CAIs, this intercept is still not as ^{16}O enriched as the Δ^{17}O value (−28.4 ± 1.8‰) inferred for the Sun based on solar wind analyses (McKeegan et al., 2011).

Magnesium Isotope Compositions

Magnesium isotope data were acquired over several analytical sessions but only the analyses made with a high-intensity primary ion beam have sufficient precision and accuracy to provide quantitative constraints on the Al-Mg systematics of 1623-5. All the magnesium isotope data, corrected for IMF, are reported on the DSM3 scale in Table 2 and plotted on the three-isotope diagram in Figure 5.

All interior phases in 1623-5 show large mass-dependent isotope fractionation effects with δ^{25}Mg′ ranging from +19 to 33‰ (Figure 6); olivine is slightly less fractionated than pyroxene or melilite, which are similarly fractionated in the inclusion interior. Spinel was only analyzed in a few spots, but it appears to be the most fractionated of all phases in the inclusion core areas. Olivine enclosed within the pyroxene-rich area is generally more fractionated than that enclosed within the melilite-rich area, although there is almost complete

overlap in the range of δ^{25}Mg′ values measured. There is no olivine remaining in the igneous rim, but in the melilite there has a range of δ^{25}Mg′ values like that of olivine; pyroxene is more fractionated (δ^{25}Mg′ > 29‰) and a single analysis of spinel yielded δ^{25}Mg′ = +39‰. A limited number of analyses of phases in the accretionary rim shows a wide range of magnesium isotope fractionation. Coarse-grained spinel and hibonite intergrown with spinel (Figure 2a) are highly fractionated (δ^{25}Mg′ > 35‰) but the fine-grained spinel near the border with Vigarano matrix material shows only limited mass fractionation, typical of that seen in many CV CAIs (δ^{25}Mg′ ~4–5‰). The range of mass-dependent isotopic fractionation of magnesium in all phases in 1623-5 is consistent with the bulk interior and mantle values reported by Davis et al. (1991), δ^{25}Mg = +30.6 ± 0.3‰ and δ^{25}Mg = +28.9 ± 2.6‰, respectively.

Data that were acquired with the high-intensity beam (Session 1) for all spots showing high amounts of magnesium mass fractionation (i.e., all except for the fine-grained material filling the vesicle) are plotted on the Al-Mg evolution diagram in Figure 7a, where δ^{26}Mg* values represent residuals after correction for mass-dependent fractionation occurring during evaporative loss of magnesium (Equation 4; see Davis et al., 2015). Although showing considerable scatter, there is nevertheless a positive correlation between δ^{26}Mg* and ^{27}Al/^{24}Mg, providing evidence for the presence of radiogenic ^{26}Mg in at least some portions of 1623-5. The coarse-grained oxide phases (spinel, hibonite) present in the accretionary rim show well-resolved excesses (positive δ^{26}Mg* values), whereas the olivine in both portions of the inclusion core have consistent and distinctive negative δ^{26}Mg* values. A weighted mean of the 10 olivine analyses yields δ^{26}Mg* = −0.48 ± 0.02‰ (MSWD = 0.93) which, given the low Al concentration of forsterite, must represent the initial

TABLE 3. Silicon isotopic compositions of Vigarano 1623-5.

Spot #	Mineral	$\delta^{30}Si$ (‰)	2σ	$\delta^{29}Si$ (‰)	2σ
Pyroxene-rich area					
9-D10	Olivine	12.40	1.22	7.06	0.72
11-F11	Olivine	17.62	0.90	n.a.	n.a.
9-J11	Olivine	15.39	0.58	7.45	0.28
10-J11	Olivine	16.44	0.58	8.50	0.24
6-J11	Olivine	12.63	0.40	6.38	0.32
7-J11	Olivine	20.20	0.56	10.57	0.36
8-J11	Olivine	22.44	0.82	n.a.	n.a.
11-J11	Olivine	34.53	0.32	17.39	0.20
7O	Olivine	19.01	0.46	9.82	0.28
7Si-J11	Olivine	5.12	1.22	3.17	0.74
34-F11	Olivine	6.79	1.10	4.22	0.74
11-J11	Olivine	8.31	1.24	5.41	0.74
13-F11	Olivine	9.56	1.22	5.56	0.74
18-F11	Olivine	6.27	1.22	3.80	0.74
22-F11	Olivine	23.24	1.36	12.83	1.20
20-J11	Pyroxene	13.17	0.70	n.a.	n.a.
23-J11	Pyroxene	30.49	0.34	n.a.	n.a.
Melilite-rich area					
4-J11	Olivine	14.33	0.98	6.57	0.40
1-J11	Olivine	11.84	0.50	5.95	0.38
3-J11	Olivine	11.90	0.44	5.75	0.26
2-J11	Olivine	9.32	0.34	4.62	0.36
5-J11	Olivine	7.52	0.56	3.59	0.36
43-D10	Olivine	9.06	1.10	5.38	0.72
44-D10	Olivine	7.68	1.10	4.7	0.74
20-F11	Olivine	17.90	1.00	n.a.	n.a.
15-J11	Melilite	11.75	1.18	n.a.	n.a.
16-J11	Melilite	13.42	1.20	n.a.	n.a.
17-J11	Melilite	17.62	1.18	n.a.	n.a.
24-J11	Melilite	15.90	1.18	n.a.	n.a.
Igneous rim					
1	Melilite	6.88	1.20	n.a.	n.a.
2	Melilite	22.27	1.20	n.a.	n.a.
3	Melilite	25.28	1.20	n.a.	n.a.
7	Melilite	26.20	1.22	n.a.	n.a.
9	Melilite	9.13	1.22	n.a.	n.a.
6	Melilite	18.25	1.20	n.a.	n.a.
8	Melilite	22.87	1.18	n.a.	n.a.
10	Melilite	6.82	1.30	n.a.	n.a.
14	Melilite	15.69	1.18	n.a.	n.a.
19	Melilite	10.50	1.20	n.a.	n.a.
15	Melilite	11.75	1.18	n.a.	n.a.
16	Melilite	13.42	1.20	n.a.	n.a.
17	Melilite	17.62	1.18	n.a.	n.a.
18	Melilite	15.90	1.18	n.a.	n.a.
Chondrule					
1	Olivine	5.21	0.68	n.a.	n.a.
2	Olivine	5.29	0.48	n.a.	n.a.
3	Olivine	5.40	0.52	n.a.	n.a.
14	Olivine	5.03	0.48	n.a.	n.a.
15	Olivine	5.19	0.28	n.a.	n.a.
16	Olivine	5.34	0.56	n.a.	n.a.

TABLE 3. *Continued.* Silicon isotopic compositions of Vigarano 1623-5.

Spot #	Mineral	$\delta^{30}Si$ (‰)	2σ	$\delta^{29}Si$ (‰)	2σ
17	Olivine	5.29	0.60	n.a.	n.a.
23	Olivine	5.69	0.56	n.a.	n.a.
10	Olivine	5.06	0.60	n.a.	n.a.
11	Olivine	5.34	0.40	n.a.	n.a.
46	Olivine	5.27	0.36	n.a.	n.a.
47	Olivine	5.06	0.64	n.a.	n.a.

Abbreviation: n.a., not analyzed.

magnesium isotope composition of Vigarano 1623-5. That this FUN inclusion should exhibit an initial magnesium isotope anomaly (prior to evaporation and/or ^{26}Al decay) is not surprising and is consistent with bulk data that show a deficit of ^{26}Mg of $-17 \pm 3\varepsilon$ (Loss et al., 1994), although a quantitative comparison would require consideration of the mass-fractionation correction "law" used by Loss et al. (1994).

Neither the pyroxene-rich nor the melilite-rich interior areas have phases with high enough Al/Mg to reveal evidence for in situ decay of ^{26}Al; however, when the aluminum-rich melilite data from the igneous rim are included, then a positive correlation appears for both the pyroxene- and melilite-rich portions. If the average of the olivine data is considered to represent the initial magnesium composition of 1623-5 and neglecting data for small spinel grains in the inclusion interior, which could be susceptible to isotopic exchange of magnesium with surrounding phases (e.g., Sheng et al., 1992), then a clear correlation is seen between $\delta^{26}Mg*$ and $^{27}Al/^{24}Mg$ for the remaining data including those in the accretionary rim (Figure 7b). A least-squares fit to the data yields initial $^{26}Al/^{27}Al = 1.6 \times 10^{-5}$, but with considerable scatter (MSWD = 9), indicating that the Al-Mg system is significantly disturbed. Nevertheless, we conclude that, unlike the case for many FUN CAIs (MacPherson et al., 1995) but similar to Allende CMS-1 (Williams et al., 2017), ^{26}Al was not negligible with a lower bound on $^{26}Al/^{27}Al$ of approximately 1×10^{-5} at the time that phases in the interior and the rims of 1623-5 attained isotopic closure.

Silicon Isotope Compositions

Silicon isotopic compositions were determined on 38 spots in the pyroxene-rich part, the melilite-rich part, and the igneous rim of 1623-5 revealing a wide variability. A plot of $\delta^{29}Si'$ vs. $\delta^{30}Si'$ in olivine (Figure 8) has a slope consistent with 0.5, demonstrating that the silicon isotopic variations are due to mass-dependent fractionation (Molini-Velsko et al., 1986). The correlation line is also consistent with Rayleigh distillation from an intercept
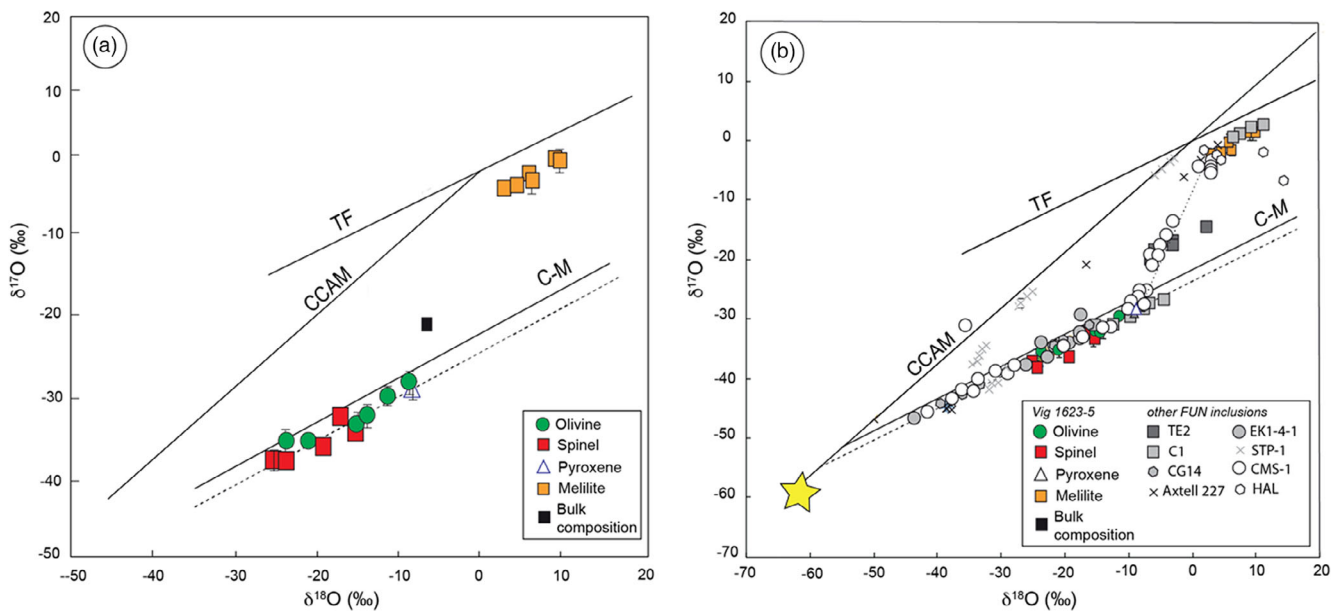
FIGURE 4. Oxygen isotope compositions of phases in 1623-5, plotted as $\delta^{17}O$ versus $\delta^{18}O$. a) Data for 1623-5 only; bulk composition from Davis et al. (1991). Spinel, pyroxene, and olivine all disperse along a line of slope ~0.5, parallel to but slightly displaced from the original FUN line as defined by Clayton and Mayeda (line C-M). Melilite data also plot along a slope ~0.5 line, but near the upper end of the Carbonaceous Chondrite Anhydrous Mineral (CCAM) line and just below the Terrestrial Fractionation (TF) line. b) Oxygen isotopes in 1623-5 in comparison with data for selected other FUN inclusions (Krot et al., 2014; Williams et al., 2017) and composition inferred for the Sun from captured solar wind (star symbol; McKeegan et al., 2011).

(initial $\delta^{29}Si$ value) of 0.3‰ as found by Davis et al. (1991). Olivine and melilite show $\delta^{30}Si$ values ranging from +5.1‰ to +34.5‰ within the inclusion core (Table 3; Figure 9). Two spots measured on pyroxene (from the pyroxene-rich portion) have $\delta^{30}Si$ values of +13.2‰ and +30.5‰. Olivine from the melilite-rich part shows a smaller range and slightly less fractionated $\delta^{30}Si$ values than does olivine from the pyroxene-rich part. However, there is a large overlap of the silicon isotope compositions of the different parts of the inclusion (Figure 9). Interior melilite is less fractionated and displays more homogeneous silicon isotope compositions than does melilite from the igneous rim. The overall range of silicon isotope compositions is consistent with the bulk isotope analysis of 1623-5 by Davis et al. (1991), $\delta^{30}Si = +20.3$‰, $\delta^{29}Si = +10.5$‰.

DISCUSSION

Forsterite-bearing CAIs are rare and have long been recognized as special due to their proclivity to exhibit FUN characteristics. As one of the only "classical" FUN inclusions which still exists in thin section, 1623-5 has been well studied by in situ methods for mineralogy, chemistry, and magnesium and silicon isotopes (Davis et al., 1991). In recent years, FUN inclusions have additionally been studied in situ for

oxygen isotopes (Krot et al., 2010, 2014; Thrane et al., 2008; Williams et al., 2017), but this study is the first to incorporate analyses of oxygen, magnesium, and silicon isotopes in a FoB/FUN CAI. With this work and the prior results of Davis et al. (1991), there now exist ~220 isotopic analyses on this complex, heterogeneous object that, together with constraints derived from experimental studies of isotopic fractionation during volatilization (e.g., Mendybaev et al., 2006, 2013, 2017, 2021), can bring information regarding the origin of 1623-5 and its formation environment. An important part of this puzzle is deciphering the possible relationship(s) between the various parts of the inclusion, specifically between the two FoB interior "core" areas—one rich in pyroxene and the other in melilite. In addition, there is the problem of the origin of the igneous rim and the nature of the materials overlying it in the accretionary rim.

Davis et al. (1991) previously showed that, although Vigarano 1623-5 is an igneous object, its core (i.e., both the pyroxene-rich part and the melilite-rich part) and mantle (i.e., the olivine-free igneous rim) are petrologically incompatible and could not have crystallized from a homogeneous melt. They therefore argued that the igneous rim of 1623-5 required melt volatilization from the surface of the CAI during a
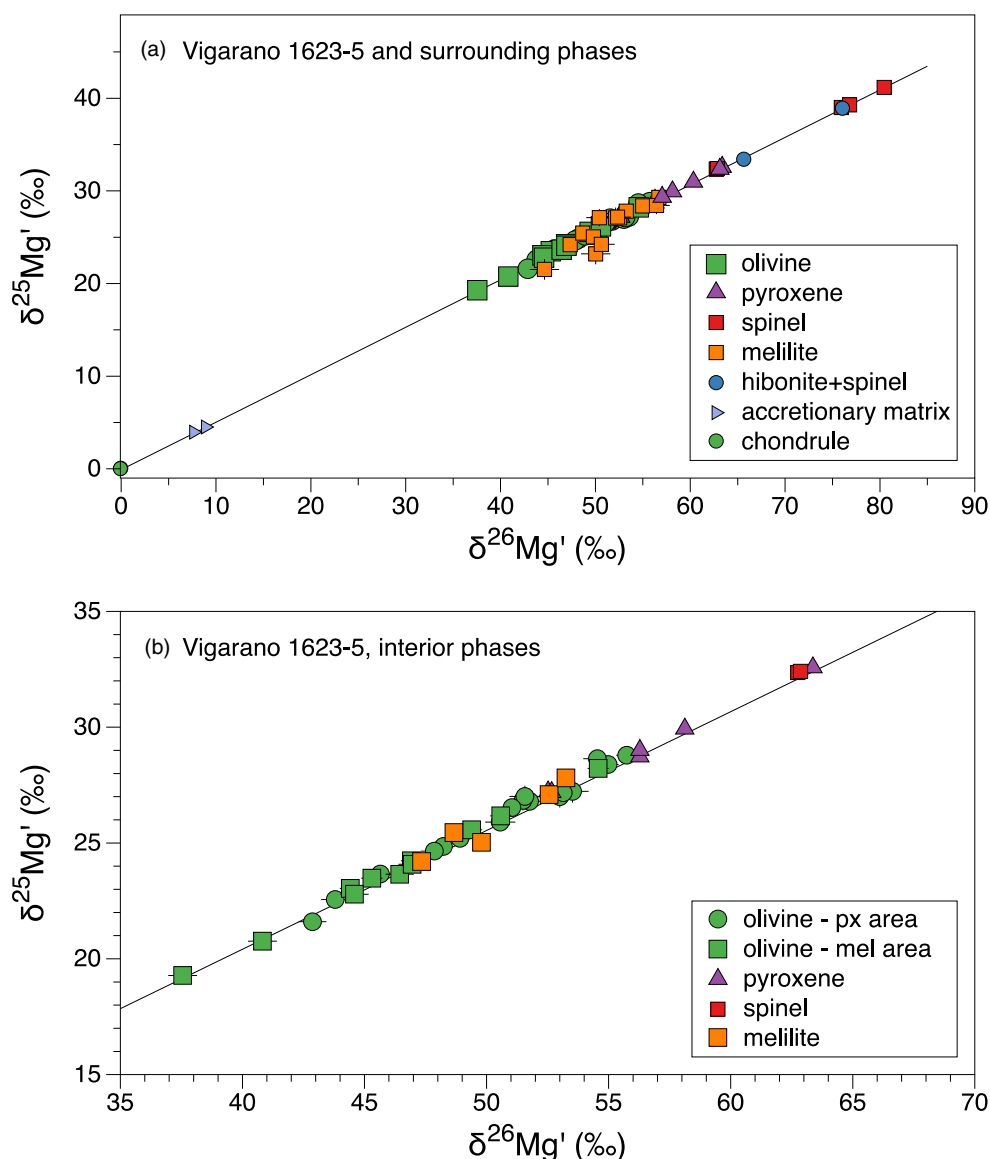
FIGURE 5. Mg isotope data for 1623-5 relative to DSM3. a) All phases measured in the inclusion interior, the igneous rim, and the accretionary rim material are designated by mineral type. Also shown are two analyses of a porphyritic olivine chondrule adjacent to Vigarano 1623-5; b) only phases from the inclusion interior. The line shown in both panels is the mass-dependent fractionation line derived from evaporation experiments with slope = 0.5128 (Davis et al., 2015).

subsequent heating event that was sufficiently rapid as to leave most of the core relatively unaffected. The environment and timing of such an event was unconstrained by the existing data and possible models for the formation of the FoB parts of 1623-5 were noted to exhibit some inconsistencies between petrographic and isotopic constraints. In the following discussion, we explore further the Davis et al.'s (1991) model in light of our new data. In particular, we address the following questions:

1. What is the relationship between the two parts of 1623-5 and the igneous rim? What are the implications for the composition and nature of the precursor of 1623-5?

2. Under what conditions was the igneous rim formed? What is the relationship between the igneous rim and the overlying accretionary material?

3. What can we infer about the relationships between 1623-5 and other FUN inclusions, in particular its isotopic twin C1? What distinguishes the precursors
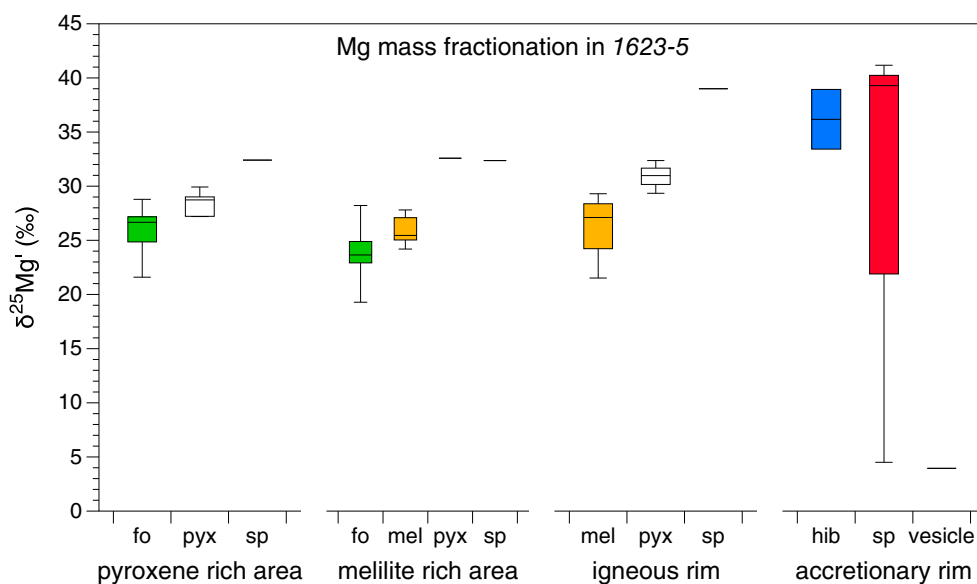
FIGURE 6. Box plot depicting the range of mass-dependent Mg isotopic fractionation values by phase and location in 1623-5. Shown are the median, first and third quartiles, and maximum and minimum in each phase analyzed.

and/or formation environments of FUN inclusions from those of "normal" igneous CAIs lacking FUN characteristics?

Igneous Formation of the Inclusion Interior Parts

The dominant features of the central regions of 1623-5 are coarse-grained, euhedral forsterite crystals enclosed either in fassaitic pyroxene or in åkermanitic ($Åk_{89}$) melilite in two separate, distinct lithologies (Figure 1) with all phases showing isotopically heavy, mass-fractionated magnesium and silicon (Figures 5 and 8). The range of mass fractionation ($\delta^{25}Mg'$ and $\delta^{30}Si'$) observed in olivine is extensive and overlaps without significant difference between the pyroxene-rich and the melilite-rich parts (Figures 6 and 9), suggesting a common history. As concluded by Davis et al. (1991), the texture and the high degree of mass fractionation point to igneous crystallization from a melt that had previously (or concurrently) undergone large amounts of magnesium and silicon loss due to volatilization.

As discussed by Davis et al. (1991), a melt with the inferred bulk composition of 1623-5 will first crystallize spinel and/or olivine, followed by melilite and then pyroxene (see their figure 19 and below). Indeed, the presence of clusters of spinel crystals enclosed in pyroxene, melilite, or, occasionally, olivine, suggests that spinel was the first phase to crystallize (Davis et al., 1991). In the melilite-rich part, olivine is poikilitically enclosed in melilite, however, when pyroxene crystallization starts, olivine not armored by melilite should begin reacting with the melt, producing

melilite and pyroxene. This process implies that euhedral olivine should be found only in melilite, whereas small, rounded olivine grains would occur wherever pyroxene is present. This is not the case (Figure 1). A possible explanation, favored by Davis et al. (1991), is that the true bulk composition of 1623-5 is not well represented by the available thin section (which is obviously a fragment of a larger, heterogeneous object). The true bulk of 1623-5 can also represent a mix between the late evaporative process and the legacy of the precursor.

The discrepancy between expected and observed crystallization paths could also reflect kinetic effects due to different nucleation rates for pyroxene and melilite. Our oxygen isotope data, measured on phases in only the pyroxene-rich part, confirm that isotopic fractionation continued to progress during fractional crystallization (Figure 4a) in the sequence spinel, olivine, and then pyroxene as found experimentally by Mendybaev et al. (2013); the oxygen isotopic composition of melilite is discussed below. Significant differences in isotopic compositions of O, Mg, and Si between different minerals are expected if each mineral crystallized from still-evaporating melts. The large range of O, Mg, and Si isotope compositions in different mineral phases is likely indicative of fast crystallization of melt that experienced heating and evaporation at earlier stages. This is consistent with olivine being generally less fractionated than pyroxene and melilite, although there is considerable overlap with the latter (Figures 6 and 9). However, attempting to reconcile the isotopic record with the detailed petrographic observations shows that this is not a simple story of single-stage fractional crystallization to
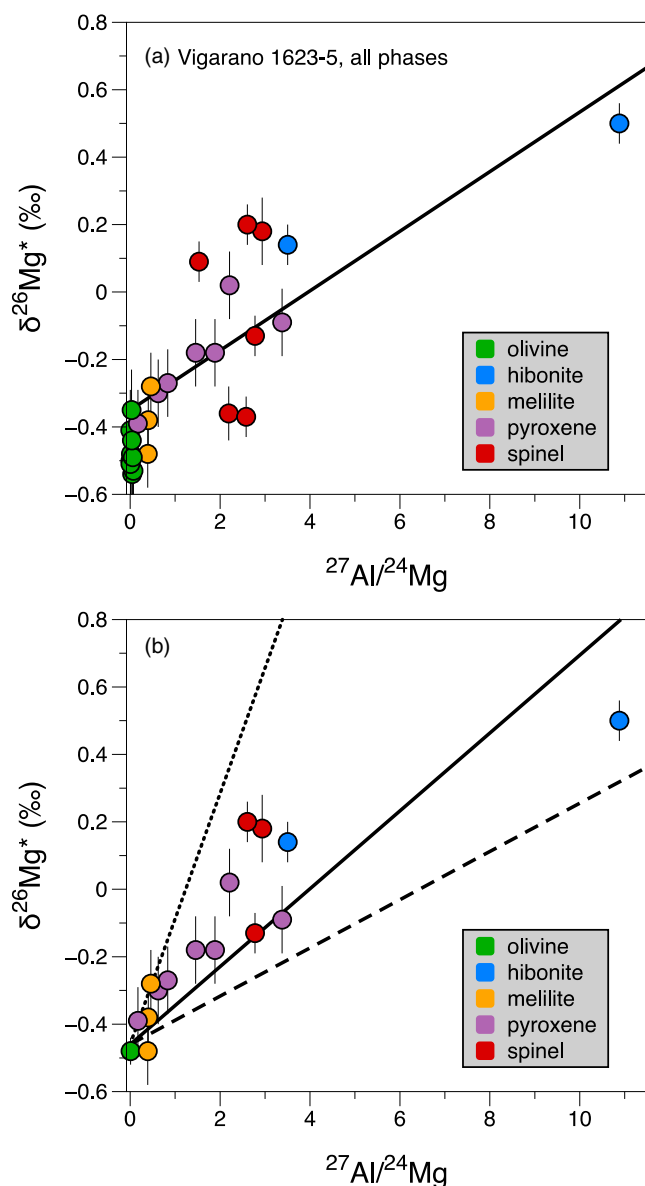
FIGURE 7. a) Al-Mg evolution diagram for all phases of 1623-5 that show high degrees of Mg mass fractionation (i.e., not including the vesicle and matrix). The best fit line has a slope corresponding to an initial $^{26}Al/^{27}Al = 1.2 \times 10^{-5}$ and an intercept $= -0.34‰$, but with excessive scatter (MSWD = 18); b) Al-Mg evolution diagram including average olivine composition and removing interior spinel grains. The best fit line has slope corresponding to $^{26}Al/^{27}Al = 1.6 \times 10^{-5}$ but still does not represent an isochron (MSWD = 9). The dotted line corresponds to a canonical $^{26}Al/^{27}Al = 5.2 \times 10^{-5}$ with initial $\delta^{26}Mg^*$ equivalent to that of olivine, and the dashed line corresponds to $^{26}Al/^{27}Al = 1 \times 10^{-5}$. Error bars are 2σ.

produce both parts of the inclusion interior during a common melting event. Finally, we note the obvious fact that the pyroxene-rich and melilite-rich lithologies have different bulk chemical compositions, so the crystallization sequence could have been different in different portions of the CAI. The fact that the two parts of the "core" of 1623-5 share similar isotopic properties for magnesium and silicon (and probably oxygen, but this is not known), means only that they both underwent significant evaporative loss while molten, not that they both had to have shared a common melt.

The magnesium and silicon isotopic correlation lines shown in Figures 5 and 8, respectively, are consistent with fractionation via Rayleigh distillation (see discussion in Davis et al., 2015) suggesting, to first order, that a single fractionation factor characterizes evaporation (for each element) from a continuously well-mixed melt. However, the fraction of magnesium vs. silicon lost by evaporation in 1623-5 calculated from the Rayleigh equation for the observed $\delta^{25}Mg'$ and $\delta^{30}Si'$ is not consistent with expectations, implying a higher evaporation fraction for magnesium than for silicon. A series of experiments has been conducted to investigate the evaporation of CAI-like melts under various conditions of pressure, temperature, and composition in order to try to reproduce both the chemical and isotope compositions of FUN inclusions (Mendybaev et al., 2013, 2017, 2021). A comparison of the measured isotopic compositions of 1623-5 forsterite with pure forsterite residues of evaporation experiments utilizing compositions of FUN inclusions (including 1623-5 and C1) shows large discrepancies (Figure 10). This suggests that in considering a melt with a bulk composition close to the estimated 1623-5 precursor (see below), a single evaporation event cannot fully explain the magnesium and silicon isotope compositions recorded by olivine. More complex processes appear to be required, even for the interior parts of 1623-5, possibly involving multiple heating events potentially with different cooling rates.

Figure 11 illustrates the basic model of Davis et al. (1991) along with what we now know from experiments about the evaporation of a melt of 1623-5 bulk core composition. Such a melt will have forsterite as its liquidus phase, followed closely by spinel (Figure 11). Simple crystallization of such a melt will thus follow the shaded gray arrows, proceeding from the bulk composition directly away from olivine that contains ~1.5% CaO. Upon reaching the olivine-melilite boundary curve (point "A" on the figure), magnesium-rich melilite ($Åk_{~60-70}$) will join the crystallization sequence, and eventually so also will calcic pyroxene. Davis et al. (1991) attempted to estimate the effects of melt volatilization, based on limits for the relative evaporation rates of SiO versus MgO (shown as dotted red arrows in Figure 11a that correspond to SiO/MgO = 0.65 and 0.82, respectively). These limits are imposed by the absence of monticellite and pyroxene from the igneous rim assemblage of 1623-5, and the presence of aluminous
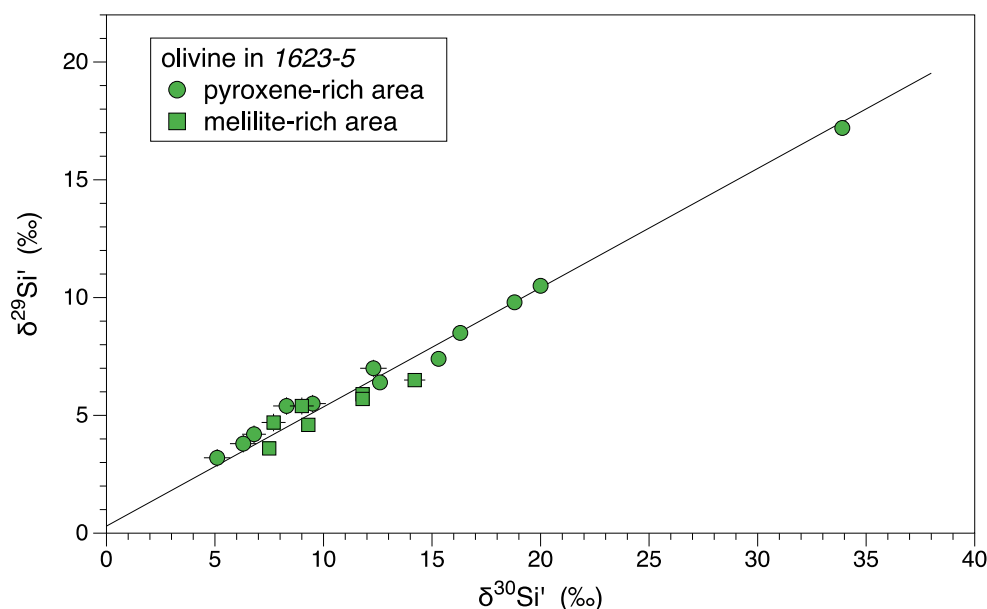
FIGURE 8. Silicon 3-isotope plot for olivine in Vigarano 1623-5 according to location in the inclusion. The line depicts Rayleigh fractionation assuming ideal kinetic isotope fractionation of evaporating SiO and an intercept of $\delta^{29}Si = 0.3‰$ as in Davis et al. (1991).
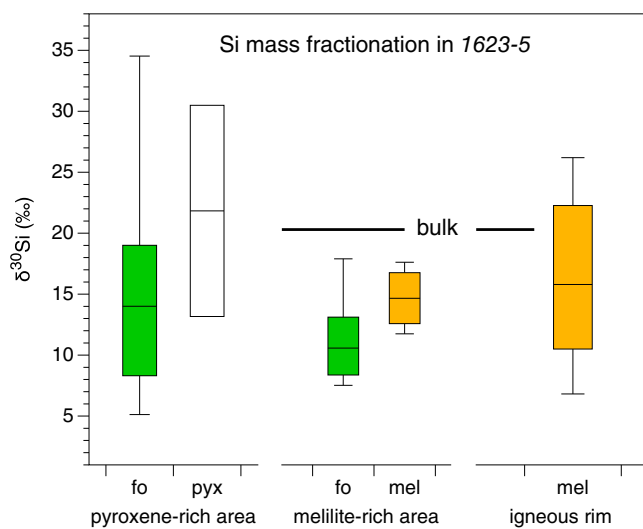

FIGURE 9. Box plot of $\delta^{30}Si$ according to mineral phase and location in Vigarano 1623-5-5. Also shown is the bulk $\delta^{30}Si$ of the inclusion, 20.3‰ (Davis et al., 1991).

composition (Ivanova et al., 2018). In fact, Mendybaev et al. (2017) demonstrated experimentally that the evaporation of a 1623-5 melt (solid red arrow in Figure 11a) is different from the one envisioned by Davis et al. (1991) and does not even enter the melilite field at all. This is entirely contrary to the constraints noted by the latter authors, yet those constraints cannot be ignored. From a purely petrologic point of view, the only way to reconcile the Mendybaev et al.'s (2017) results with the constraints noted by Davis and co-workers is if olivine crystallization occurred simultaneously with melt evaporation. A combination of olivine crystallization and residual melt evaporation would lead to a curved melt evolution path such as illustrated schematically by the green arrows in Figure 11b, causing the melt to encounter the melilite-olivine boundary curve. At that point, the igneous rim and inclusion interior liquids follow different paths ("M" and "C," respectively, in Figure 11b) because the core composition still maintains a composition from which both olivine and melilite crystallize, whereas the igneous rim evolves into the melilite field and causing olivine to begin to react to form åkermanite. Eventually, the åkermanite itself dissolves into the melt. This results in the formation of separate inner and outer igneous rims (Figures 12 and 13), where the inner igneous rim retains the olivine "ghosts" described by Davis et al. (1991) but in the outer igneous rim they have been erased entirely.

Spatial information corroborates the complexity of the melt processes resulting in the core regions of the inclusion. Figure 12 shows a pattern of increasing mass
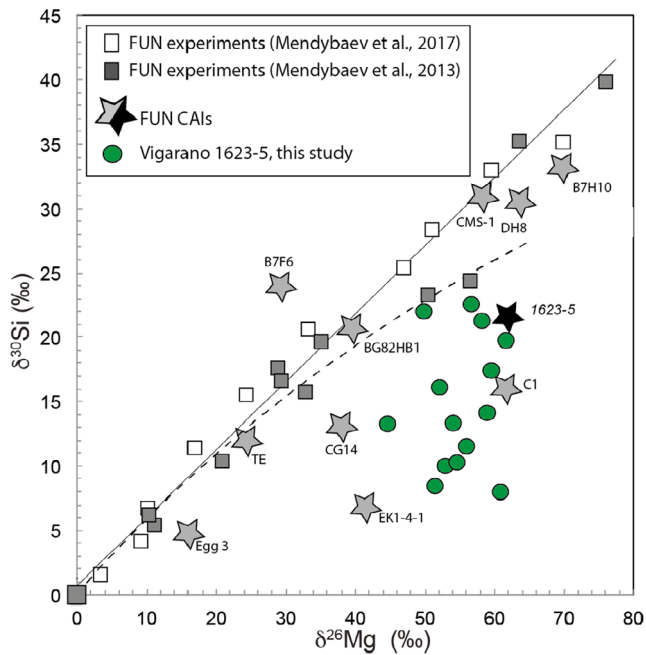
melilite. In the Davis et al. (1991) model, based on the observation of end-member åkermanite pseudomorphically replacing olivine, the loss of magnesium and silicon drives the residual melt *beyond* the olivine-melilite boundary curve and into the melilite field, where the equilibrium melilite composition is significantly more aluminous than that in the CAI core. However, recent experimental and theoretical work has shown that the SiO_2/MgO ratio during melt evaporation is dependent on bulk

FIGURE 10. $\delta^{30}Si$ versus $\delta^{26}Mg$ of individual olivine grains from the interior of 1623-5 (in green) and of experimental evaporation FUN residues (figure adapted from Mendybaev et al., 2013, 2017) in black and white. The bulk compositions of some other FUN inclusions are also plotted (stars, Brigham, 1990; Clayton et al., 1988; Mendybaev et al., 2017). Olivine grains from 1623-5, similar to most of the FUN inclusions, are not aligned with the experimental trend determined from free evaporation of forsterite. Note that the experimental data shown are for completely molten forsteritic melt (not forsterite) and that the isotopic evaporation trajectories might be quite different for mellitic melt (see fig. 5 in Mendybaev et al., 2013). In the case of evaporation of a crystallizing melt, the melt composition can become more SiO_2 or MgO rich depending on which minerals crystallize, affecting the activities of SiO_2 and MgO in the melt as well as the Mg and Si isotope evolution during evaporation. Oxygen isotope compositions demonstrate that 1623-5 was indeed crystallizing during evaporation, potentially explaining the wide range of Si and Mg isotope composition observed.

fractionation of both magnesium and silicon recorded by forsterite as a function of position. In the melilite-rich part of the inclusion, both $\delta^{26}Mg'$ and $\delta^{30}Si'$ increase outward toward the igneous rim; note that we are not considering the trend in the rim here because it is devoid of olivine. Because olivine should not crystallize from the inclusion interior outward, this implies that the trend does not simply reflect progressive crystallization during ongoing volatilization, but rather that the olivine inherited a mass-fractionated compositional gradient that had already been imposed in the melt droplet. This gradient was not erased during the last melting event producing the melilite-rich part, nor that responsible for the igneous rim. Such a gradient in the melt could also imply chemical gradients, thus leading to complexities in

comparing to experiments. Although data are limited, the same trend is not observed in the pyroxene-rich part of 1623-5 (see Figure S4). Additional complications could arise due to heterogeneous nucleation and crystallization on refractory grains that might lead to different fractionation factors for both magnesium and silicon isotopes (Tachibana, 2001) which would be interesting to reproduce in laboratory. Despite these complexities, it is worth noting that evaporation experiments do adequately reproduce the estimated oxygen isotope fractionation of FUN inclusions, including 1623-5 and C1 (Mendybaev et al., 2017). The same experiments (Mendybaev et al., 2017) also reproduce the mass fractionation for magnesium and silicon in the FUN inclusions TE, BG82HB1, and CMS-1; however, these are not FoB inclusions (nor is C1).

Formation of the Igneous Rim

The main parts of 1623-5 are partially layered by a refractory, olivine-free rim that consists primarily of highly zoned melilite (Figure 1) which is much more aluminum-rich than the $Åk_{89}$ interior melilite. In the pyroxene-rich part, the igneous rim melilite compositions range from ~$Åk_{89–75}$ at the inner edge (adjacent to the "core") to ~$Åk_{40}$ near the rim's outer edge; isolated grains, just beyond the rim, are even more aluminum rich, down to $Åk_{16}$ (Davis et al., 1991). Our analyses of magnesium and silicon isotopic compositions of the melilite, and of other minor phases (pyroxene, spinel) associated with the rim, show very high degrees of mass fractionation (Tables 2 and 3), ranging from ~23‰ to 39‰ per amu for magnesium (Figures 6 and 12) and ~3‰ to 13‰ per amu for silicon (Figures 9 and 12), which are in agreement with the average values reported for "mantle" phases by Davis et al. (1991). These chemical and isotopic compositions clearly indicate crystallization of the rim during evaporation of a melt layer. However, as previously discussed, such a rim cannot have crystallized from a single evolving melt of bulk 1623-5 or from an equilibrium melt of either the melilite-rich or pyroxene-rich parts (Davis et al., 1991).

Petrographic evidence that the igneous rim formation involved a highly dynamic, disequilibrium event (i.e., 'flash heating') is apparent in Figure 13. As first pointed out by Davis et al. (1991), at the inner boundary of the rim pure åkermanite grains can be seen pseudomorphically replacing forsterite creating the so-called "ghost" crystals as the olivine dissolved into the melt (Figure 13). The magnesium and silicon added to the melt were then progressively evaporated resulting in a strong chemical gradient in the melt layer and the eventual crystallization of highly zoned melilite once the temperature dropped. Isotopic profiles across the rim partially confirm this scenario but raise some additional questions.
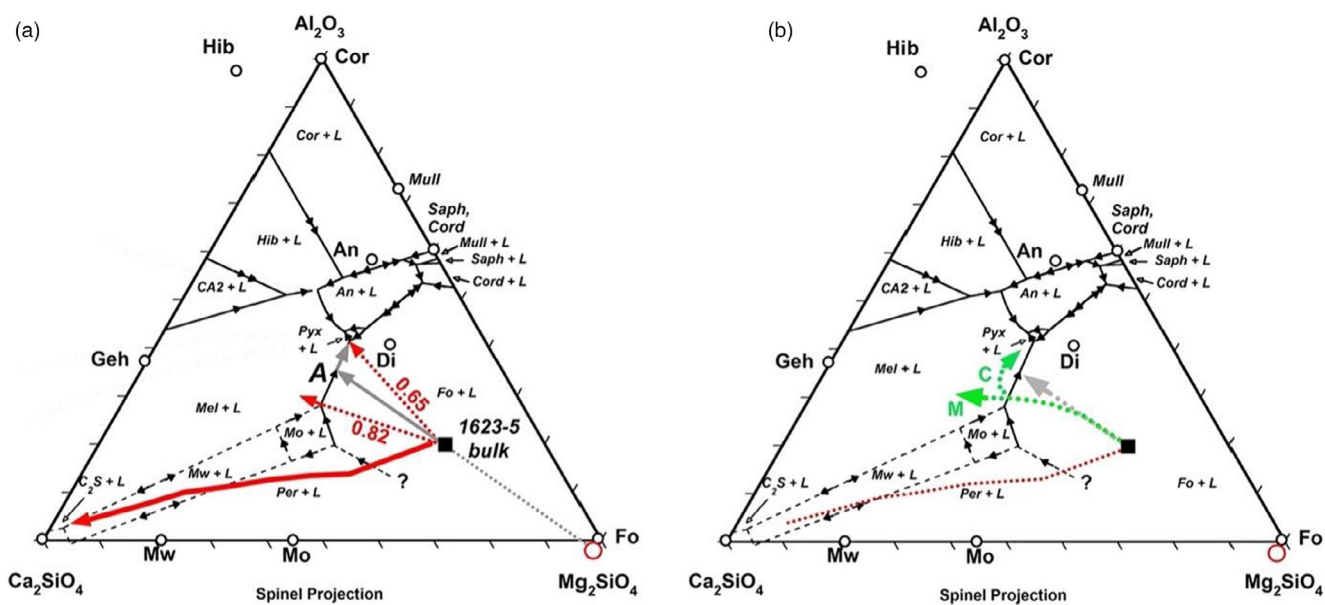
FIGURE 11. a) Crystallization and melt volatilization paths for a melt having the bulk composition of the core of Vigarano 1623-5, as postulated by Davis et al. (1991). The solid gray arrows show the path for simple crystallization of a melt having the composition of Vigarano 1623-5 (black square). The dotted red arrows show the limiting cases for evaporation trajectories based on the constraints given by Davis et al. (1991; their figure 19), corresponding to evaporating SiO/MgO ratios of 0.65 and 0.82. In contrast, the solid red arrow is the experimentally determined trajectory for a 1623-5 melt undergoing evaporation of MgO and SiO (Mendybaev et al., 2017). The complete disconnect between the predicted vs. experimental evaporation paths of Vigarano 1623-5 requires that the 1623-5 melt must have significantly crystallized olivine prior to the onset of major evaporation, such that the resulting evaporation trajectory entered the melilite field rather than bypassing it. The open red circle near the Forsterite apex marks the composition of the olivine in 1623-5, which contains ~1.5 wt% CaO. b) Our proposed actual crystallization and evaporation trajectory for 1623-5, which accounts both for the experimental result of Mendybaev et al. and the requirement that melilite must crystallize after olivine. Note that interior inclusion crystallization ("C") follows a different trajectory than does the igneous rim ("M"), because the mantle is olivine free. An, anorthite; CA2, grossite; C₂S, α Ca$_2$SiO$_4$; Cor, corundum; Cord, cordierite; Di, diopside; Fo, forsterite; Geh, gehlenite; Hib, hibonite; L, liquid (melt); Mel, melilite solid solution; Mo, monticellite; Mu, mullite; Mw, merwinite; Per, periclase; Pyx, pyroxene solid solution; Saph, sapphirine.
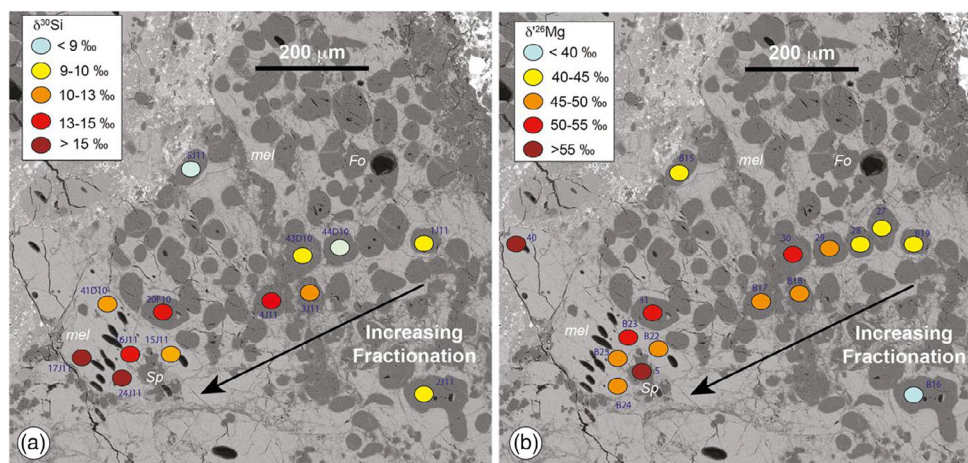

FIGURE 12. BSE image of the melilite-rich area with the isotopic composition for Si (a) and for Mg (b) reported using a color chart, red for the most mass-fractionated composition, blue for the least mass-fractionated composition. Mineral phases are labeled in white, Fo for forsterite, and mel for melilite. There is a trend from the inside to the outer part of this melilite-rich part. Forsterites show a range of ~10‰ for δ^{30}Si and ~ 17‰ for δ′^{26}Mg, in both cases increasing from the inside of the CAI to its exterior. The spot numbers are labeled in blue.
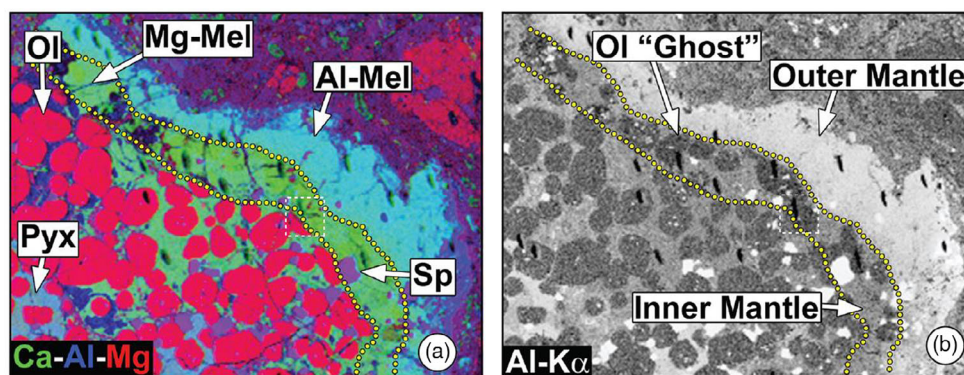
FIGURE 13. a) Combined elemental X-ray map (Mg-red, Ca-green, Al-blue) zoomed on the pyroxene-rich core and showing the relationship between olivine and the melilite igneous rim. The rim shows a chemical gradient from a magnesium-rich inner part to an aluminum-rich exterior. b) Aluminum X-ray map of the pyroxene-rich core and the boundary with the igneous rim. Note the presence of olivine ghosts in the inner part of the olivine-free igneous rim.

Figure 14 shows magnesium, silicon, and oxygen isotopic compositions made in several traverses across the melilite igneous rim from the interior of the pyroxene-rich area to the edge of the rim. The data are plotted as a function of åkermanite content, which is a proxy for distance and extent of evaporation across the melt layer (e.g., Figure 13). The $\delta^{30}Si$ of the melilite (Figure 14a) increases steadily by ~20‰ from the pyroxene-rich part, where it shows very little mass-dependent fractionation, to the outer edge of the igneous rim where it is highly fractionated. This increase in mass-dependent fractionation parallels a steady decrease in the åkermanite content of the melilite, which is the expected behavior for progressive distillation during evaporation. However, the situation for magnesium is not so straightforward. Although the isotopic composition of magnesium is highly mass fractionated in the melilite of the igneous rim (the mean $\delta^{26}Mg'$ value is 52‰), the profile (Figure 14b) shows no systematic change across the rim, in marked contrast to the $\delta^{30}Si$ profiles. The inconsistency between the $\delta^{26}Mg'$ and $\delta^{30}Si$ profiles may indicate faster isotopic self-diffusion of magnesium than of silicon during cooling following solidification of the igneous rim (LaTourrette & Hutcheon, 1999). Another possibility is that magnesium might diffuse quickly in the melt, which would be consistent with its very heavy isotopic composition and a lack of isotopic gradient (Richter et al., 2009). The magnesium isotopic composition measured in a few small grains of pyroxene or spinel disseminated in the igneous rim shows significantly greater mass-dependent fractionation (Figure 6) than any of the interior phases (olivine, melilite, or pyroxene) supporting the idea that a "flat" profile in the rim melilite reflects some sort of diffusive relaxation of a gradient present during evaporation and thus helping explain the discrepancy between the magnesium and silicon isotope profiles. It

would be useful to analyze more of these individual grains; however, their small size (<5 µm) presents a challenge. More experimental work, particularly on diffusion rates, is needed to fully understand these profiles.

Oxygen isotope compositions of melilite in the igneous rim show uniform $\Delta^{17}O = -3.9 \pm 0.5‰$, which contrasts strongly with the ^{16}O-rich compositions of the primary igneous phases in 1623-5 (Figure 4a). This demonstrates that the melilite has exchanged oxygen isotopes with a planetary-like oxygen reservoir, similar to that seen in melilite from other FUN inclusions (e.g., EK-1-4-1, CMS-1) and the rim material of HAL (Simon et al., 2011; Williams et al., 2017). However, unlike the melilite in CMS-1 which is homogeneous (Williams et al., 2017), the melilite of the igneous rim in 1623-5 shows a ~5‰ range in $\delta^{18}O$ that also suggests a trend with position across the rim (Figure 14). In contrast to the profile seen in silicon, the highest $\delta^{18}O$ values are for melilite near the interior border of the igneous rim, whereas at the periphery $\delta^{18}O$ is approaching the bulk value of Vigarano (Clayton & Mayeda, 1999). Because $\delta^{18}O$ values are not mass-fractionated to extremely high values, the data clearly indicate exchange of oxygen during and/or following flash melting and volatilization of the igneous rim. The exchange reservoir could be nebular or asteroidal, for example, the Vigarano parent body, but the temperature must have been low enough as to not affect the highly mass-fractionated silicon and magnesium.

Relationships Among the Different Lithologies of 1623-5

Vigarano 1623-5 is a highly heterogeneous object with a complex history. The petrologic and isotopic data summarized above indicate that its core regions formed from precursors with distinctive compositions that suffered similar degrees of mass-dependent fractionation via evaporative loss of the abundant moderately volatile
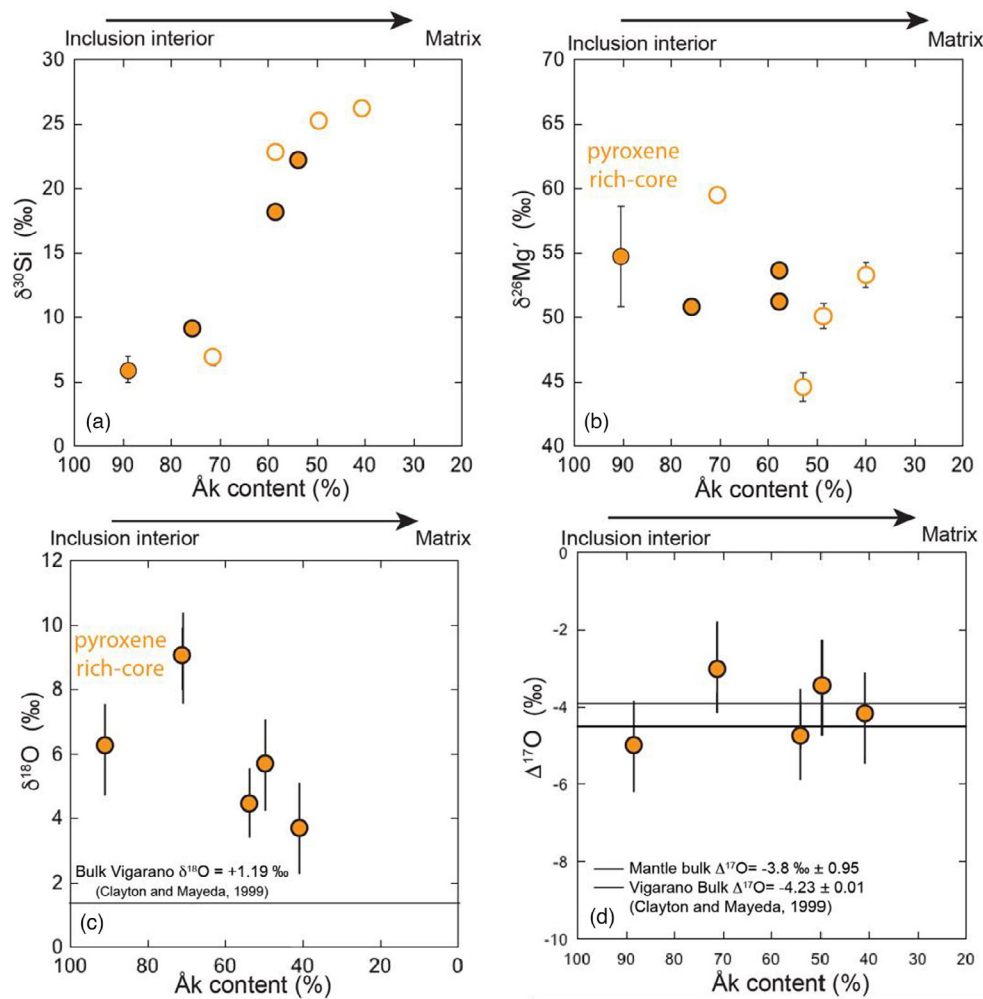
FIGURE 14. Isotopic profiles across the melilite igneous rim of Vigarano 1623-5 as a function of position and melilite composition. a) $\delta^{30}Si$; b) $\delta^{26}Mg'$; c) $\delta^{18}O$; d) $\Delta^{17}O$ versus åkermanite content from the interior of the pyroxene-rich area to the edge of the igneous rim. The bulk oxygen isotope composition of Vigarano (Clayton & Mayeda, 1999) and the melilite composition from the inside of the pyroxene-rich core (in black) are also plotted and labeled. The $\delta^{18}O$ profile shows a trend while the $\Delta^{17}O$ profile is homogeneous. The $\delta^{30}Si$ profile shows a clear evaporation trend while the $\delta^{26}Mg'$ profile does not show any correlation. Errors bars are 1σ. For Mg and Si, two different profiles have been performed and are shown in open and closed symbols, while for O, only one isotopic profile has been measured.

elements, magnesium, silicon, and oxygen, during melting, probably multiple times. The last of these melting and evaporation events was rapid and resulted in the formation of an igneous rim on both the pyroxene-rich and melilite-rich parts of the inclusion. Although it cannot be known with certainty, it is simplest to suppose that the igneous rims on both parts of the inclusion were formed simultaneously, in the same event. But the rims are discontinuous, implying breakup with partial loss of rim sections prior to reassembly of the CAI.

Among the many large igneous CAIs studied in CV chondrites, the general type of thermal and mechanical history inferred for 1623-5 is not particularly unusual, except in the degree of mass fractionation and the

remarkably high evaporative mass loss thereby implied. Many CAIs have experienced a final 'flash-heating' event, resulting in the formation of igneous Wark–Lovering rims (Wark & Lovering, 1977). What is highly unusual, and possibly unique, about 1623-5 is the large swath of mineralogically diverse materials that envelop the compact FoB cores of the inclusion. Following the lead of Davis et al. (1991), we have referred to this as an "accretionary rim," but it should be appreciated that it is not really like the typically thin, fine-grained FoB, stratified structures that are found exterior to Wark–Lovering rims on many CV CAIs. The accretionary rim of 1623-5, as exposed in the thin section, varies widely in apparent thickness from perhaps a few μm to several

hundred μm, and in texture from very fine-grained (sub-μm) material to coarse-grained igneous objects several hundred μm in size, such as the spinel–hibonite-rich objects in areas 4 and 5 (Figures 1 and 2). These diverse materials accreted together, filling the vesicles, and creating the periphery of the object that would become 1623-5. Obviously, this occurred sometime after the flash-heating event that formed the igneous rim on the pyroxene-rich and melilite-rich parts of the inclusion. Also obvious is that this accreted material is different chemically and mineralogically than "normal" matrix of carbonaceous chondrites (see Figure S1); the entire 1623-5 inclusion, with its accreted rim, is a xenolith in the Vigarano meteorite.

We can glean some insights into the nature of this material, its formation environment, and its relationship to the FoB parts of 1623-5 from isotopic properties of at least some of the coarse-grained constituents (the fine-grained materials being too small for analysis with our primary ion beam). Extremely high mass-dependent fractionation of magnesium (>35‰ per amu) is seen in the coarse-grained hibonite–spinel objects (Figure 2) found in the accretionary rim. These values are higher than the magnesium mass fractionation seen in either of the inclusion cores and are similar to the highest values found in the igneous rim. While this does not provide compelling evidence of a direct genetic relationship between these highly refractory oxide aggregates and the FoB cores of 1623-5, it nevertheless hints that they were at least formed in the same types of environments, that is from materials that had undergone extreme kinetic isotopic fractionation due to large amounts of mass loss during evaporation.

Of course, the reservoir of material forming in this environment has interesting isotopic characteristics that could, in principle, be diagnostic of a genetic relationship between all the disparate parts of 1623-5. At least nine elements in 1623-5 exhibit anomalies in one or more isotopes due to a mix of nucleosynthetic inheritance distinct from the average chondritic ("primordial") values (Loss et al., 1994). Unfortunately, data exist only for "bulk" 1623-5, meaning that the distribution of nuclear anomalies ("UN" characteristics) among the various phases and lithologies present in 1623-5 is presently not known. In particular, it is not known if any UN effects are carried by phases in the accretionary rim. However, one of the elements for which a nucleogenetic isotopic anomaly is resolved in situ in 1623-5 is magnesium. The averages of $\delta^{26}Mg^*$ of forsterite grains in both the pyroxene-rich and the melilite-rich parts of 1623-5 agree with each other, and at –0.48 ± 0.02‰ are well resolved from normal chondritic magnesium. This shared isotopic anomaly in forsterite is probably the best evidence for a common origin of the precursor material that was

thermally processed to form the melilite-rich and pyroxene-rich parts of 1623-5. If sufficient material still exists, it would be interesting to reanalyze magnesium isotopes in Allende C1 grains with higher precision to see whether initial $\delta^{26}Mg^*$ values, corrected for mass fractionation during evaporative loss of magnesium, agree with the small anomalies preserved in forsterite of Vigarano 1623-5.

Timing of Formation?

If we assume that the $\delta^{26}Mg^*$ values of forsterite represent the initial magnesium isotopic composition of the reservoir of material from which all the phases now present in 1623-5 formed, then we can infer that live ^{26}Al was present at the time of isotopic closure of objects in the accretionary rim (Figure 7) with an apparent $^{26}Al/^{27}Al$ in the range of ~1 to ~4 × 10^{-5}. Although its presence cannot be quantifiably resolved in the inclusion cores because they are too magnesium rich to yield ingrowth of sufficient radiogenic ^{26}Mg, it seems likely that there was some ^{26}Al present (at around the 10^{-5} level) at the time of formation of the igneous rim. As noted previously, the data scatter well beyond analytical uncertainty and it is not possible to infer any isochronous relationships among the various parts of the inclusion. Interestingly, the level of live ^{26}Al inferred for Vigarano 1623-5 is roughly the same as that seen in CMS-1 (Williams et al., 2017). Plagioclase mineral separates from Allende C1, the isotopic twin to 1623-5, show $^{26}Al/^{27}Al$ up to ~5 × 10^{-6} (Esat et al., 1978), which is an order of magnitude lower than the canonical value in coarse-grained Allende CAIs (Davis & McKeegan, 2014; MacPherson et al., 1995). However, Al-Mg records in plagioclase are often disturbed and, in the case of C1, the plagioclase separates also showed highly variable magnesium mass fractionation from ~0 to 30‰ per amu suggesting some contamination of the mineral separates (Esat et al., 1978). These factors, along with ambiguities due to the mass fractionation correction laws used, make it difficult to assess the level of ^{26}Al present when C1 formed. Regardless, it is clear that the modest amounts of ^{26}Al inferred for 1623-5 and CMS-1, while still below canonical levels, nevertheless far exceed those in any other FUN CAIs (Krot et al. 2012 and references therein). Chronological significance is, however, still elusive.

The low abundance of ^{26}Al in FUN CAIs is usually not attributed to late formation or later reprocessing (isotopic disturbance), owing to the perceived unlikely preservation of their nuclear anomalies in such a scenario. Thus, the existence of FUN CAIs and other ^{26}Al-poor refractory inclusions having large nucleosynthetic isotope anomalies (e.g., PLAC hibonites

in CM chondrites, Kööp et al., 2016) is often taken as evidence that they formed prior to injection and subsequent homogenization of ^{26}Al into the early Solar System. However, PLAC hibonites in CM chondrites display variable ^{26}Al/^{27}Al ratios (Liu et al., 2012) and suggest a heterogeneous Mg isotope distribution when PLACs formed.

Vigarano 1623-5 and Allende CMS-1 complicate this view somewhat because they formed when some ^{26}Al existed in the early solar system. Whether the low abundance of that nuclide in these objects means that the buildup of ^{26}Al in the solar system was gradual, or whether 1623-5 formed with a sufficient admixture of old material with "dead ^{26}Al," is not clear.

Composition of the Precursor

Because of their relatively large isotopic heterogeneities and the hypothesis that they represent the earliest formed refractory inclusions, there is considerable interest in trying to constrain models for the origin(s) of the precursor materials that formed the FUN inclusions in nebular environments characterized by high temperatures and strong evaporative loss of moderately volatile elements. Based on the isotopic results of evaporation experiments, Mendybaev et al. (2013) calculated the bulk chemical compositions of the precursors to 1623-5 and its isotopic twin, C1. Both precursors are required to be very rich in magnesium and silicon, and in the case of C1 its estimated precursor is reasonably close to a bulk composition expected for solid condensate from a solar gas. The same is not true for any plausible precursor to 1623-5. The problem is that the present composition of 1623-5 itself has a CaO/Al_2O_3 ratio that is nearly a factor of 2× higher than solar (CaO/Al_2O_3 of 1.7, see Davis et al. 1991 for details). Calcium and aluminum will not fractionate from one another during melt evaporation until all the magnesium and silicon have evaporated, so their anomalous ratio in 1623-5 must be an intrinsic property of the precursor. Mendybaev et al. concluded that the 1623-5 precursor did not form simply by melting solar nebula condensates.

A Proposed History for Vigarano 1623-5

1623-5 is a complex igneous and sedimentary object, a xenolith in the Vigarano meteorite that has recorded at least four major events during its formation history (Figure 15). The time and environment of the first event are not well constrained, but it must have involved condensation of a Mg- and Si-rich aggregate which was not in equilibrium with a gas of bulk solar composition, and which contained a large number of inherited nucleosynthetic isotopic anomalies. This precursor aggregate incorporated some ^{26}Al, likely less than the canonical level sampled by most

other (igneous and non-igneous) CAIs in CV chondrites. It formed in an ^{16}O-rich gas whose composition is preserved by the average $\Delta^{17}O = -24.5 \pm 1.0‰$ for primary minerals of the pyroxene-rich core. This value is consistent with the $\Delta^{17}O$ values of other FUN inclusions (Krot et al., 2014) and of the pre-alteration $\Delta^{17}O$ values of non-FUN CV CAIs (e.g., Krot et al., 2020). It is also similar to the $\Delta^{17}O$ values of Mg-rich Amoeboid Olivine Aggregates (AOAs, Imai & Yurimoto, 2003; Krot et al., 2002; Marrocchi, Villeneuve, et al., 2019), but is slightly more ^{17,18}O-rich than the inferred solar composition (McKeegan et al., 2011). The precursor aggregate was then strongly heated, causing a high degree of (or possibly total) melting accompanied by large amounts of evaporation of moderately volatile elements and resulting in a forsterite-rich object with strongly mass fractionated magnesium and silicon isotope compositions. Chemical and isotopic gradients appear to have been at least partially preserved, perhaps in a glassy phase in this intermediate object. The nebular condensates should have been olivine rich but quite different from AOAs. These objects display chemical and isotope heterogeneities (Marrocchi, Euverte, et al., 2019; Marrocchi, Villeneuve, et al., 2019) and are prone to be recycled several times during gas–melt interactions but do not contain large isotope anomalies. Moreover, forsterite of 1623-5 is enriched in CaO (up to 1.7 wt%, Davis et al., 1991).

Following the formation of the precursor aggregate, additional heating event(s) led to partial melting and further evaporation which continued as mineral phases crystallized in the cooling droplet with spinel and/or olivine forming first, followed by melilite and then pyroxene. The fractional crystallization occurred even as the isotopic composition of the melt was still evolving toward heavier values due to continued evaporation, evidence for which is imperfectly preserved in the mineralogical and spatial correlations with isotopic compositions of O, Mg, and Si. The vesicles must have formed at this stage, further evidence of gas loss while the CAI was at least partially molten. Thus were the primary petrogenetic features of the interior core regions of 1623-5 established, although the reason for two distinct composition core regions, one pyroxene rich and the other melilite rich, remains unexplained.

The subsequent history of 1623-5 is somewhat easier to decipher and follows the scenario put forward by Davis et al. (1991). As with many CAIs, 1623-5 suffered a "flash" heating event that melted only an outer layer which rapidly evaporated losing additional magnesium and silicon and crystallizing an olivine-free, Al-rich igneous rim. The rapidity of this last heating event is evidenced by the preservation of olivine "ghosts" at the inner melt boundary of the rim. This event must have postdated vesicle formation, as the large vesicle is lined
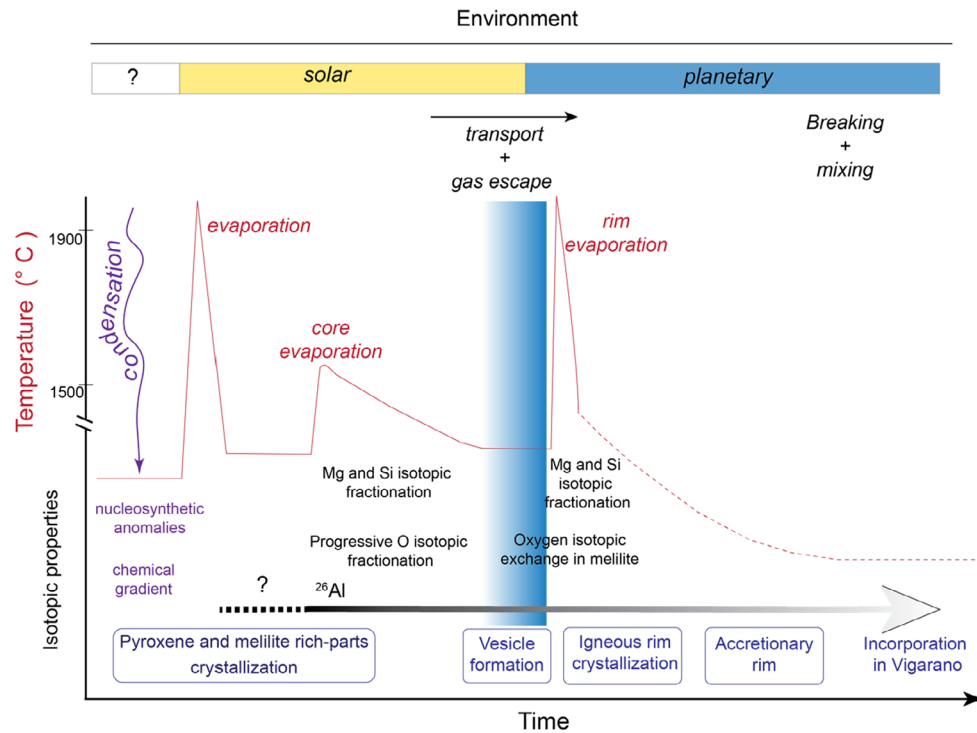
FIGURE 15. Schematic model of a possible formation scenario of FUN inclusion 1623-5, from initial condensation of a forsterite-rich precursor through several heating events that evaporated and fractionated isotopes of Mg, S, and O to final incorporation into the parent body of the Vigarano meteorite (see text for discussion).

with evaporation residue where pyroxene has broken down to melilite and perovskite. Fine-grained refractory material was then accreted by the CAI to form the accretionary rim, which filled the vesicle and grew quite thick in places. The coarse-grained igneous aggregates associated with the accretionary rim matter also show extremely mass fractionated Mg isotopic compositions indicating that these accretionary materials formed in a similar environment as the core regions of 1623-5. This is significant because it demonstrates that the fine-grained material was accreted prior to transport of 1623-5 to a region characterized by more planetary-like oxygen with $\Delta^{17}O \sim -4\permil$, as seen in the melilite of the igneous rim. However, it is not clear if this environment, in which melilite exchanged oxygen isotopes, was nebular or asteroidal. An argument for the former is that melilite oxygen shows modest but resolvable mass-dependent fractionation, possibly indicating evaporation. On the other hand, the vesicle is lined on one side with large crystals of kirschsteinite, which very likely formed during aqueous activity on a planetesimal (Davis et al., 1991). Melilite oxygen isotopic exchange could have occurred during low-temperature aqueous alteration (Wasson et al., 2001), even if such activity was relatively limited in the Vigarano meteorite parent body. Thus, the oxygen isotopic composition of melilite and

especially its apparent mass-dependent trajectory remains a puzzle.

Remaining Unresolved Issues

Despite more than 200 in situ isotopic analyses and detailed petrographic study (Davis et al., 1991, and this work), 1623-5 has not revealed all its secrets; we describe below some of the still unresolved issues.

There is the fundamental question regarding the origins of the nucleosynthetic isotopic anomalies inside 1623-5. Vigarano 1623-5 contains nucleosynthetic anomalies in a wide range of minor and trace elements including Cr, Zn, Sr, Ba, and Sm (Loss et al., 1994). However, it is notable that the largest anomalies occur as deficits in both ^{50}Ti and ^{48}Ca, which cannot be simply explained by a "carrier phase" within 1623-5 or its isotopic twin, C1 (Loss et al., 1994). An order of magnitude of larger "negative anomalies" in ^{50}Ti and ^{48}Ca are known in platy-hibonite crystals ("PLACS") of CM chondrites (Fahey et al., 1987; Ireland, 1990; Kööp et al., 2016; Zinner et al., 1986), but their relationship, if any, to FUN CAIs is obscure. Likewise, the distribution of isotope anomalies within the different petrologic units of 1623-5 remains unknown and further work is needed to find possible heterogeneities, particularly in the fine-grained

accretionary dust rimming or filling portions of the various units of 1623-5, that could be valuable for shedding light on the nature of the various presolar materials that were thermally processed to form the cores of this and other CAIs.

The origin of the isotopic similarity between C1 and 1623-5, which display comparable mass-fractionated isotope compositions and nearly identical nucleosynthetic anomalies despite very different chemical compositions, remains enigmatic. Both precursors of C1 and 1623-5 are required to be very rich in magnesium and silicon, and in the case of C1 its estimated precursor is plausibly close to a hypothetical condensate composition from a solar gas. The same is not true for any plausible precursor to 1623-5 and thus the origin and formation of the precursor of 1623-5 remain mysterious.

As already described above, the relationships between the different parts of the 1623-5 inclusion need to be better explored. The melilite- and pyroxene-rich parts are different chemically and were likely formed from different precursors. The spinel–hibonite aggregates enclosed in the accretionary rim and in the vesicle shows a very highly mass fractionated composition, suggesting a similar formation environment as the main parts of 1623-5, but it is not clear how these chemically disparate objects are related. The vesicles must have been formed when the pyroxene-rich part was still molten, before formation of the igneous rim. Indeed, the large vesicle is surrounded by an almost continuous igneous rim. The vesicles are filled by the accretionary fine-grained hibonite-rich material, which is different from the matrix of Vigarano. The filling clearly occurred after the formation of the igneous rim but before the incorporation in Vigarano. The nature and origin of the fine-grained accretionary material should be further explored in detail.

Evaporation experiments by Mendybaev et al. (2021) indicate that the time scale of a flash heating event capable of forming the igneous rim could be very rapid, 10s of minutes in a low pressure H_2 atmosphere. A plausible scenario for that kind of heating event is a shock wave process. The physical environment for such an event would likely be different than that which produced the more extensive heating and prolonged evaporation during crystallization of the main parts of the inclusion. The origin of the evaporating events recorded in 1623-5 as well as the time scales and mechanisms of transport between different nebular environments remain under-constrained.

Additional questions arise regarding the residence of 1623-5 in the cooler parts of the solar nebula, following high temperature processing and prior to accretion into a planetesimal. If 1623-5 was formed very early in the solar nebula, prior to arrival and/or homogenization of ^{26}Al,

then how did it survive with a unique accretionary rim? This porous, composite structure consists of very fine-grained, almost dusty material and nevertheless coexists with coarse-grained minerals that appear to be more robust. The entire inclusion has been fragmented as evidenced by the partial loss of the igneous rim. In such a context, how were these materials transported and stored until after chondrule formation, so potentially during 1–2 million years? Of course, this is merely an example of the well-known general problem regarding the preservation of CAIs as nebular components for most of the duration of the solar nebula, but it is perhaps exacerbated by those "early" objects, like 1623-5 and other inclusions that contain nucleosynthetic anomalies and low ^{26}Al (see Ciesla et al., 2010; Yang & Ciesla, 2012). Is it possible that small, early planetesimals could have existed? An objection to the solution of an early "parent body" for CAI storage is that such an early-formed asteroid would necessarily melt because of the presence of ^{26}Al. But if ^{26}Al was introduced later into the solar nebula, that is, after formation of the earliest (FUN and PLAC) CAIs, such an early "FUN asteroid" could happily accrete and never melt. Alternatively, the idea of early formation of FUN inclusions may not be right. Perhaps a "late" inheritance of nucleosynthetic anomalies was accompanied (in carrier grains) by an increased proportion of "dead" Al; however, even such a scenario still requires processing in a high temperature environment characterized by solar-like oxygen.

CONCLUSIONS

Vigarano 1623-5 is a unique object that has recorded an interesting and complex history, likely at the early stages of formation of the solar system.

1. The Vigarano 1623-5 FUN CAI displays the most highly mass-fractionated magnesium and silicon isotopic compositions recorded in meteorites that can only be explained by kinetic isotopic fractionation effects during extensive evaporation events.
2. The core interior and igneous rims of 1623-5 have different chemical and isotopic compositions and have therefore been formed during different events of heating and evaporation.
3. Vigarano 1623-5 is one of the few FUN inclusions that contained live ^{26}Al, albeit at less than canonical levels, which likely implies an early origin of the inclusion.
4. The different oxygen isotope compositions between the core and the igneous rim imply at least two different stages of evolution: the first stage involved melt crystallization in a solar-like reservoir, and the second stage resulted in exchange of oxygen in the melilite igneous rim with a planetary-like reservoir.

5. The precursor of 1623-5 was probably a forsterite-rich aggregate with pre-existing nuclear anomalies and chemical gradients that were preserved even after multiple episodes of melting and strong evaporation. The relation of this FoB FUN inclusion to its isotopic twin FUN inclusion C1 and to other refractory phases (e.g., PLAC hibonites) with large nucleosynthetic isotopic anomies in several elements remains a puzzle.

Data Availability Statement—The data that support the findings of this study are available from the corresponding author upon reasonable request.

Editorial Handling—Dr. Yves Marrocchi

REFERENCES

Aléon, J., Marin-Carbonne, J., McKeegan, K. D., and El Goresy, A. 2018. O, Mg, and Si Isotope Distributions in the Complex Ultrarefractory CAI Efremovka 101.1: Assimilation of Ultrarefractory, FUN, and Regular CAI Precursors. *Geochimica et Cosmochimica Acta* 232: 48–81.

Amelin, Y., Kaltenbach, A., Iizuka, T., Stirling, C. H., Ireland, T. R., Petaev, M., and Jacobsen, S. B. 2010. U-Pb Chronology of the Solar System's Oldest Solids with Variable $^{238}U/^{235}U$. *Earth and Planetary Science Letters* 300: 343–50.

Brigham, C. A. 1990. Isotopic Heterogeneity in Calcium-Aluminum-Rich Meteoritic Inclusions. California Institute of Technology, PhD thesis.

Bullock, E. S., MacPherson, G. J., Nagashima, K., Krot, A. N., Petaev, M. I., Jacobsen, S. B., and Ulyanov, A. A. 2012. Forsterite-Bearing Type B Refractory Inclusions from CV3 Chondrites: From Aggregates to Volatilized Melt Droplets. *Meteoritics & Planetary Science* 47: 2128–47.

Ciesla, F. J. 2010. The Distributions and Ages of Refractory Objects in the Solar Nebula. *Icarus* 208: 455–67.

Clayton, R. N., Hinton, R. W., and Davis, A. M. 1988. Isotopic Variations in the Rock-Forming Elements in Meteorites. *Philosophical Transactions of the Royal Society of London. Series A, Mathematical and Physical Sciences* 325: 483–501.

Clayton, R. N., MacPherson, G. J., Hutcheon, I. D., Davis, A. M., Grossman, L., Mayeda, T. K., Molini-Velsko, C., Allen, J. M., and El Goresy, A. 1984. Two Forsterite-Bearing FUN Inclusions in the Allende Meteorite. *Geochimica et Cosmochimica Acta* 48: 535–48.

Clayton, R. N., and Mayeda, T. K. 1977. Correlated Oxygen and Magnesium Isotope Anomalies in Allende Inclusions. 1. Oxygen. *Geophysical Research Letters* 4: 295–8.

Clayton, R. N., and Mayeda, T. K. 1999. Oxygen Isotope Studies of Carbonaceous Chondrites. *Geochimica et Cosmochimica Acta* 63: 2089–104.

Clayton R. N., Mayeda T. K., and Epstein S. 1978. Isotopic Fractionation of Silicon in Allende Inclusions. 9th Lunar and Planetary Science Conference, abstract #1066, pp. 1267–78.

Clayton, R. N., Onuma, N., Grossman, L., and Mayeda, T. K. 1977. Distribution of the Pre-Solar Component in Allende and Other Carbonaceous Chondrites. *Earth and Planetary Science Letters* 34: 209–24.

Connelly, J. N., Bizzarro, M., Krot, A. N., Nordlund, Å., Wielandt, D., and Ivanova, M. A. 2012. The Absolute Chronology and Thermal Processing of Solids in the Solar Protoplanetary Disk. *Science* 338: 651–5.

Davis, A. M., Macpherson, G. J., Clayton, R. N., Mayeda, T. K., Sylvester, P. J., Grossman, L., Hinton, R. W., and Laughlin, J. R. 1991. Melt Solidification and Late-Stage Evaporation in the Evolution of a FUN Inclusion from the Vigarano C3V Chondrite. *Geochimica et Cosmochimica Acta* 55: 621–37.

Davis A. M., and McKeegan K. D. 2014. Short-Lived Radionuclides and Early Solar System Chronology. In *Meteorites and Cosmochemical Processes*, edited by A. M. Davis, Vol. 1 Treatise on Geochemistry, 2nd ed (Exec. Eds H. D. Holland and K. K. Turekian), 361–95. Oxford: Elsevier.

Davis, A. M., McKeegan, K. D., and MacPherson, G. J. 2000. Oxygen-Isotopic Compositions of Individual Minerals from the FUN Inclusion Vigarano 1623-5. *Meteoritics & Planetary Science* 35: A47.

Davis, A. M., Richter, F. M., Mendybaev, R. A., Janney, P. E., Wadhwa, M., and McKeegan, K. D. 2015. Isotopic Mass Fractionation Laws and Their Effects on ^{26}Al-^{26}Mg Systematics in Solar System Materials. *Geochimica et Cosmochimica Acta* 158: 245–61.

Desch, S. J., Dunlap, D. R., Dunham, E. T., Williams, C. D., and Mane, P. 2023. Statistical Chronometry of Meteorites. I. The Pb-Pb Age of the Solar System's t = 0. *Arxiv*. https://doi.org/10.48550/arXiv.2212.00390

Esat, T. M., Lee, T., Papanastassiou, D. A., and Wasserburg, G. J. 1978. Search for ^{26}Al Effects in the Allende FUN Inclusion C1. *Geophysical Research Letters* 5: 807–10.

Fahey, A. J., Goswami, J. N., McKeegan, K. D., and Zinner, E. 1987. ^{26}Al, ^{244}Pu, ^{50}Ti, REE, and Trace Element Abundances in Hibonite Grains from CM and CV Meteorites. *Geochimica et Cosmochimica Acta* 51: 329–50.

Fahey, A. J., Goswami, J. N., McKeegan, K. D., and Zinner, E. K. 1987. O-16 Excesses in Murchison and Murray Hibonites—A Case Against a Late Supernova Injection Origin of Isotopic Anomalies in O, Mg, Ca, and TI. *The Astrophysical Journal* 323: L91–5.

Galy, A., Yoffe, O., Janney, P. E., Williams, R. W., Cloquet, C., Alard, O., Halicz, L., et al. 2003. Magnesium Isotope Heterogeneity of the Isotopic Standard SRM980 and New

Reference Materials for Magnesium-Isotope-Ratio Measurements. *Journal of Analytical Atomic Spectrometry* 18: 1352–6.

Grossman, L. 1975. Petrography and Mineral Chemistry of Ca-Rich Inclusions in the Allende Meteorite. *Geochimica et Cosmochimica Acta* 39: 438–51.

Grossman, L., Ebel, D. S., and Simon, S. B. 2002. Formation of Refractory Inclusions by Evaporation of Condensate Precursor. *Geochimica et Cosmochimica Acta* 66: 145–61.

Imai, H., and Yurimoto, H. 2003. Oxygen Isotopic Distribution in an Amoeboid Olivine Aggregate from the Allende CV Chondrite: Primary and Secondary Processes. *Geochimica et Cosmochimica Acta* 67: 765–72.

Ireland, T. R. 1990. Presolar Isotopic and Chemical Signatures in Hibonite-Bearing Refractory Inclusions from the Murchison Carbonaceous Chondrite. *Geochimica et Cosmochimica Acta* 54: 3219–37.

Ivanova M. A., Mendybaev R. A., Shornikov S. I., Ryazantsev K. M., and MacPherson G. J. 2018. Evaporation of Spinel-Rich CAI Melts: A Possible Link to CH-CB CAIs. 49th Lunar and Planetary Science Conference, abstract #1965, 2 pp.

Knight, K. B., Kita, N. T., Mendybaev, R. A., Richter, F. M., Davis, A. M., and Valley, J. W. 2009. Silicon Isotopic Fractionation of CAI-Like Vacuum Evaporation Residues. *Geochimica et Cosmochimica Acta* 73: 6390–401.

Kööp, L., Davis, A. M., Nakashima, D., Park, C., Krot, A. N., Nagashima, K., Tenner, T. J., Heck, P. R., and Kita, N. T. 2016. A Link Between Oxygen, Calcium and Titanium Isotopes in ^{26}Al-Poor Hibonite-Rich CAIs from Murchison and Implications for the Heterogeneity of Dust Reservoirs in the Solar Nebula. *Geochimica et Cosmochimica Acta* 189: 70–95.

Krot, A. N., Makide, K., Nagashima, K., Huss, G. R., Ogliore, R. C., Ciesla, F. J., Yang, L., Hellebrand, E., and Gaidos, E. 2012. Heterogeneous Distribution of ^{26}Al at the Birth of the Solar System: Evidence from Refractory Grains and Inclusions. *Meteoritics & Planetary Science* 47: 1948–79.

Krot, A. N., McKeegan, K. D., Leshin, L. A., MacPherson, G. J., and Scott, E. R. 2002. Existence of an ^{16}O-Rich Gaseous Reservoir in the Solar Nebula. *Science* 295: 1051–4.

Krot, A. N., Nagashima, K., Ciesla, F. J., Meyer, B. S., Hutcheon, I. D., Davis, A. M., Huss, G. R., and Scott, E. R. D. 2010. Oxygen Isotopic Composition of the Sun and Mean Oxygen Isotopic Composition of the Protosolar Silicate Dust: Evidence from Refractory Inclusions. *The Astrophysical Journal* 713: 1159–66.

Krot A. N., Nagashima K., Lyons J. R., Lee J.-E., and Bizzarro M. (2020) Oxygen Isotopic Heterogeneity in the Early Solar System Inherited from the Protosolar Cloud. *Science Advances* 6: eaay2724 (7 pp).

Krot, A. N., Nagashima, K., Wasserburg, G. J., Huss, G. R., Papanastassiou, D., Davis, A. M., Hutcheon, I. D., and Bizzarro, M. 2014. Calcium-Aluminum-Rich Inclusions with Fractionation and Unknown Nuclear Effects (FUN CAIs): I. Mineralogy, Petrology, and Oxygen Isotopic Compositions. *Geochimica et Cosmochimica Acta* 145: 206–47.

LaTourrette, T., and Hutcheon, I. D. 1999. Mg Diffusion in Melilite: Thermal Histories for CAIs and Their Parent Bodies. 30th Lunar and Planetary Science Conference, abstract #2003, p. 2003.

Lee, T., Papanastassiou, D. A., and Wasserburg, G. J. 1976. Demonstration of ^{26}Mg Excess in Allende and Evidence for ^{26}Al. *Geophysical Research Letters* 3: 41–4.

Lee, T., Russell, W. A., and Wasserburg, G. J. 1979. Ca Isotopic Anomalies and the Lack of Aluminum-26 in an Unusual Allende Inclusion. *The Astrophysical Journal* 228: L93–8.

Leshin, L. A., McKeegan, K. D., Carpenter, P. K., and Harvey, R. P. 1998. Oxygen Isotopic Constraints on the Genesis of Carbonates from Martian Meteorite ALH84001. *Geochimica et Cosmochimica Acta* 62: 3–13.

Liu, M. C., Chaussidon, M., Göpel, C., and Lee, T. 2012. A Heterogeneous Solar Nebula as Sampled by CM Hibonite Grains. *Earth and Planetary Science Letters* 327: 75–83.

Liu, M.-C., McKeegan, K. D., Goswami, J. N., Marhas, K. K., Sahijpal, S., Ireland, T. R., and Davis, A. M. 2009. Isotopic Records in CM Hibonites: Implications for Timescales of Mixing of Isotope Reservoirs in the Solar Nebula. *Geochimica et Cosmochimica Acta* 73: 5051–79.

Loss, R. D., Lugmair, G. W., Davis, A. M., and MacPherson, G. J. 1994. Isotopically Distinct Reservoirs in the Solar Nebula: Isotope Anomalies in Vigarano Meteorite Inclusions. *The Astrophysical Journal* 436: 193–6.

MacPherson G. J. 2014. Calcium-Aluminum-Rich Inclusions in Chondritic Meteorites. In *Meteorites and Cosmochemical Processes*, edited by A. M. Davis. Vol. 1 Treatise on Geochemistry 2nd ed. (Exec. Eds. H. D. Holland and K. K. Turekian), Elsevier, Oxford, 139–79.

MacPherson, G. J., Davis, A. M., Laughlin, J. R., and Hinton, R. W. 1984. Isotopic Heterogeneity in a Forsterite-Rich FUN Inclusion. *Meteoritics* 22: 451–3.

MacPherson, G. J., Davis, A. M., and Zinner, E. K. 1995. The Distribution of Aluminum-26 in the Early Solar System—A Reappraisal. *Meteoritics* 30: 365–86.

Marin-Carbonne, J., Chaussidon, M., and Robert, F. 2012. Micrometer-Scale Chemical and Isotopic Criteria (O and Si) on the Origin and History of Precambrian Cherts: Implications for Paleo-Temperature Reconstructions. *Geochimica et Cosmochimica Acta* 92: 129–47.

Marin-Carbonne, J., McKeegan, K. D., Davis, A. M., and MacPherson, G. J. 2011. In-Situ Investigation of Silicon Isotope Compositions in a FUN Inclusion. 42nd Lunar and Planetary Science Conference, abstract #2765, 2 pp.

Marin-Carbonne, J., McKeegan, K. D., Davis, A. M., MacPherson, G. J., Mendybaev, R. A., and Richter, F. M. 2011a. Mg and Si Isotopic Compositions of Vigarano FUN Inclusion 1623-5. *Meteoritics & Planetary Science* 46: A147, #5383.

Marin-Carbonne J., McKeegan K. D., Davis A. M., MacPherson G. J., Mendybaev R. A., and Richter F. M. 2011b. O, Si and Mg Isotopic Compositions of FUN Inclusion Vigarano 1623-5. Workshop on Formation of the First Solids in the Solar System. LPI Contribution No. 163, #9083.

Marin-Carbonne J., McKeegan K. D., Davis A. M, MacPherson G. J., Mendybaev R. A., and Richter F. M. 2012. O, Si and Mg Isotopic Compositions of FUN Inclusion Vigarano 1623-5. 43rd Lunar and Planetary Science Conference, abstract #1687, 2 pp.

Marrocchi, Y., Euverte, R., Villeneuve, J., Batanova, V., Welsch, B., Ferrière, L., and Jacquet, E. 2019. Formation of CV Chondrules by Recycling of Amoeboid Olivine Aggregate-Like Precursors. *Geochimica et Cosmochimica Acta* 247: 121–41.

Marrocchi, Y., Villeneuve, J., Jacquet, E., Piralla, M., and Chaussidon, M. 2019. Rapid Condensation of the First Solar System Solids. *Proceedings of the National Academy of Sciences of the United States of America* 116: 23461–6.

McKeegan, K. D., Chaussidon, M., and Robert, F. 2000. Incorporation of Short-Lived [10]Be in a Calcium-Aluminium-Rich Inclusion from the Allende Meteorite. *Science* 289: 1334–7.

McKeegan K. D., Davis A. M., Taylor D. J., and MacPherson G. J. 2005. In Situ Investigation of Mg Isotopes Composition in a FUN Inclusion. 36th Lunar and Planetary Science Conference, abstract #2007, 2 pp.

McKeegan, K. D., Kallio, A. P. A., Heber, V. S., Jarzebinski, G., Mao, P. H., Coath, C. D., Kunihiro, T., et al. 2011. The Oxygen Isotopic Composition of the Sun Inferred from Captured Solar Wind. *Science* 332: 1528–32.

Mendybaev, R. A., Kamibayashi, M., Teng, F. Z., Savage, P. S., Georg, R. B., Richter, F. M., and Tachibana, S. 2021. Experiments Quantifying Elemental and Isotopic Fractionations During Evaporation of CAI-Like Melts in Low-Pressure Hydrogen and in Vacuum: Constraints on Thermal Processing of CAIs in the Protoplanetary Disk. *Geochimica et Cosmochimica Acta* 292: 557–76.

Mendybaev, R. A., Richter, F. M., and Davis, A. M. 2006. Crystallization of Melilite from CMAS-Liquids and the Formation of the Melilite Mantle of Type B1 CAIs: Experimental Simulations. *Geochimica et Cosmochimica Acta* 70: 2622–42.

Mendybaev, R. A., Richter, F. M., Georg, R. B., Janney, P. E., Spicuzza, M. J., Davis, A. M., and Valley, J. W. 2013. Experimental Evaporation of Mg- and Si-Rich Melts: Implications for the Origin and Evolution of FUN CAIs. *Geochimica et Cosmochimica Acta* 123: 368–84.

Mendybaev, R. A., Williams, C. D., Spicuzza, M. J., Richter, F. M., Valley, J. W., Fedkin, A. V., and Wadhwa, M. 2017. Thermal and Chemical Evolution in the Early Solar System as Recorded by FUN CAIs: Part II—Laboratory Evaporation of Potential CMS-1 Precursor Material. *Geochimica et Cosmochimica Acta* 201: 49–64.

Molini-Velsko, C., Mayeda, T. K., and Clayton, R. N. 1986. Isotopic Composition of Silicon in Meteorites. *Geochimica et Cosmochimica Acta* 50: 2719–26.

Park, C., Nagashima, K., Krot, A. N., Huss, G. R., Davis, A. M., and Bizzarro, M. 2017. Calcium-Aluminum-Rich Inclusions with Fractionation and Unidentified Nuclear Effects (FUN CAIs): II. Heterogeneities of Magnesium Isotopes and [26]Al in the Early Solar System Inferred from In Situ High-Precision Magnesium-Isotopic Measurements. *Geochimica et Cosmochimica Acta* 201: 6–24.

Piralla, M., Villeneuve, J., Schnuriger, N., Bekaert, D. V., and Marrocchi, Y. 2023. A unified chronology of dust formation in the early solar system. *Icarus* 394: 15427.

Richter, F. M., Dauphas, N., and Teng, F. Z. 2009. Non-Traditional Fractionation of Non-Traditional Isotopes: Evaporation, Chemical Diffusion and Soret Diffusion. *Chemical Geology* 258: 92–103.

Sahijpal, S., and Goswami, J. N. 1998. Refractory Phases in Primitive Meteorites Devoid of [26]Al and [41]Ca: Representative Samples of First Solar System Solids? *The Astrophysical Journal Letters* 509: L137–40.

Sheng, Y. J., Wasserburg, G. J., and Hutcheon, I. D. 1992. Self-Diffusion of Magnesium in Spinel and in Equilibrium Melts: Constraints on Flash Heating of Silicates. *Geochimica et Cosmochimica Acta* 56: 2535–46.

Simon, J. I., Hutcheon, I. D., Simon, S. B., Matzel, J. E. P., Ramon, E. C., Weber, P. K., Grossman, L., and DePaolo, D. J. 2011. Oxygen Isotope Variations at the Margin of a CAI Records Circulation Within the Solar Nebula. *Science* 331: 1175–8.

Simon, S. B., McKeegan, K. D., Ebel, D. S., and Grossman, L. 2000. Complexly Zoned Cr-Al Spinel Found In Situ in the Allende Meteorite. *Meteoritics & Planetary Science* 35: 215–27.

Tachibana, S. 2001. Kinetic Effects on Evaporation and Condensation of Mg-Silicate Dust Particles Moving in the Turbulent Protoplanetary Disk. *Proceedings of the Japan Academy, Series B* 77: 37–42.

Thrane, K., Nagashima, K., Krot, A. N., and Bizzarro, M. 2008. Discovery of a New FUN CAI from a CV Carbonaceous Chondrite: Evidence for Multistage Thermal Processing in the Protoplanetary Disk. *The Astrophysical Journal Letters* 680: L141–L1444.

Villeneuve, J., Chaussidon, M., Marrocchi, Y., Deng, Z., and Watson, E. B. 2019. High-Precision in Situ Silicon Isotopic Analyses by Multi-Collector Secondary Ion Mass Spectrometry in Olivine and Low-Calcium Pyroxene. *Rapid Communications in Mass Spectrometry* 33: 1589–97.

Wark, D. A., and Lovering, J. F. 1977. Marker Events in the Early Evolution of the Solar System—Evidence from Rims on Ca-Al-Rich Inclusions in Carbonaceous Chondrites. 8th Lunar and Planetary Science Conference, abstract #1336, pp. 95–112.

Wasserburg, G. J., Lee, T., and Papanastassiou, D. A. 1977. Correlated O and Mg Isotopic Anomalies in Allende Inclusions: II Magnesium. *Geophysical Research Letters* 4: 299–302.

Wasson, J. T., Yurimoto, H., and Russell, S. S. 2001. ^{16}O-Rich Melilite in CO3.0 Chondrites: Possible Formation of Common, ^{16}O-Poor Melilite by Aqueous Alteration. *Geochimica et Cosmochimica Acta* 65: 4539–49.

Williams, C. D., Ushikubo, T., Bullock, E. S., Janney, P. E., Hines, R. R., Kita, N. T., Hervig, R. L., MacPherson, G. J., Mendybaev, R. A., and Richter, F. M. 2017. Thermal and Chemical Evolution in the Early Solar System as Recorded by FUN CAIs: Part I – Petrology, Mineral Chemistry, and Isotopic Composition of Allende FUN CAI CMS-1. *Geochimica et Cosmochimica Acta* 201: 25–48.

Yang, L., and Ciesla, F. J. 2012. The Effects of Disk Building on the Distributions of Refractory Materials in the Solar Nebula. *Meteoritics & Planetary Science* 47: 99–119.

Young, E. D., and Galy, A. 2004. The Isotope Geochemistry and Cosmochemistry of Magnesium. *Reviews in Mineralogy and Geochemistry* 55: 197–230.

Zinner, E. K., Fahey, A. J., Goswami, J. N., Ireland, T. R., and McKeegan, K. D. 1986. Large Ca-48 Anomalies Are Associated with Ti-50 Anomalies in Murchison and Murray Hibonites. *The Astrophysical Journal* 311: L103–7.

SUPPORTING INFORMATION

Additional supporting information may be found in the online version of this article.

Data S1. Supplementary Material.